A thermo-mechanical analysis of stainless steel structures in fire

Mian Zhou[a,*], Rui P.R. Cardoso[a], Hamid Bahai[a], Asif Usmani[b]

[a]*Department of Mechanical and Aerospace Engineering, Brunel University London, Kingston Lane, Uxbridge, UB8 3PH, UK*
[b]*Department of Building Services Engineering, The Hong Kong Polytechnic University, Hong Kong, China*

Abstract

A novel multi-dimensional combined isotropic-kinematic plasticity material model was recently developed by the authors for thermo-mechanical analysis of steels at elevated temperatures. In this paper, the capability of the new material model was further validated for transient loading conditions during both heating and cooling using recent experimental data. The multi-dimensional material model was adapted to a 1D J2 plasticity model and implemented as a uniaxial material model in the open source software OpenSEES for studying structural performance of stainless steel beam and frame structures in fire using finite element analysis (FEA). This paper presents the findings of the studies, with a focus on the behavioural comparisons between the carbon steel and the stainless steel structures. Using the FEA method, the studies provided results that filled the research gap in understanding the global structural fire performance of stainless steel structural systems. The significant impact of stainless steels' high material non-linearity and high thermal expansion on their structural fire performance is highlighted.

Keywords: stainless steel structures in fire, combined isotropic-kinematic hardening material model, thermo-mechanical analysis, OpenSEES

*Corresponding author
Email address:* `mian.zhou@yahoo.com` (Mian Zhou)

1. Introduction

The development of structural design codes, standards and specifications for stainless steel has been a research focus of academics and industry since early 1960s. The first American specification dealing with the design of structural stainless steel members was published in 1968 by the American Iron and Steel Institute (AISI) [1]. In Europe, the first edition of the design manual for structural stainless steel was published in 1994. Since then, several European research projects have been carried out to analyse the performance of structural stainless steel, resulting in the publishing of the Design Manual for Structural Stainless Steel (DMSSS). The latest (fourth) edition of the DMSSS [2] was published in 2017.

Large scale fire tests of carbon steel structures, such as Cardington tests [3], have revealed significant difference between global structural behaviour in fire and isolated structural components tested in the furnace. The testing of the behaviour of steel sub-assemblies and frame structures in a fire is extremely expensive and one single test provides only a limited amount of data. The current research gap in understanding stainless steel structural systems in fire can be approached economically and efficiently using finite element analysis (FEA); by taking advantage of existing experimental observations and experiences using FEA on large carbon steel structures in fire.

This paper investigates stainless steel structural behaviour in fire using finite element (FE) modelling, focusing on comparisons between carbon steel and stainless steel structures, and exploring potential advantages offered by the stainless steel materials during the heating stage of a fire. The influence of highly nonlinear material behaviour of stainless steel on its structural performance in fire is highlighted, the impact of higher thermal expansion of stainless steel is also discussed. Due to limited available testing data for stainless steel structures at elevated temperatures, the FE models developed and used in this project were validated against existing testing data of normal (carbon) steel structures in fire.

The accuracy of FE models is strongly dependent on the material model adopted. A novel multi-dimensional material model was recently developed by Zhou et al. [4] for thermo-mechanical analysis of steels at elevated temperatures, and implemented in an Abaqus Umat subroutine. In this paper, the capability of the new model in modelling the unloading/reloading behaviour and capturing the Bauschinger effect and transient hardening behaviour was further validated for transient loading conditions during both heating and cooling using recent experimental data of stainless steel 1.4301 (304) obtained by Ohno et al. [5]. For the comparison study of stainless steel structural behaviour, the multi-dimensional material model of Zhou et al. [4] was adapted to a one-dimensional J2 plasticity model and implemented as a uniaxial

material model in the FE software OpenSEES [6].

2. Stainless steel material characteristics

2.1. At room temperature

At room temperature, unlike the perfect elastic plastic carbon steel, stainless steel is characterised by a nonlinear stress-strain curve, exhibiting a high degree of plasticity between the proof stress and the ultimate tensile stress. Studies [7, 8, 9] in the past have also shown that an elastic perfectly plastic analysis for stainless steel leads to erroneous results.

The Bauschinger effect observed in material's response can be accounted for using the Bauschinger ratio, which is defined as in Equation (1) .

$$\vartheta = \frac{Y_{iso}}{Y_{1D}} \tag{1}$$

where Y_{iso} is the proportion of isotropic hardening. Y_{1D} is the total hardening. At the starting point of the stress-strain curve there is only isotropic hardening, so $Y_{iso} = Y_{1D} \Rightarrow \vartheta = 1.0$.

At room temperature, Silvestre et al. [10] experimentally evaluated the Bauschinger ratio (B.R.) of Austenitic 1.4404 (316L) stainless steel and ferritic 1.4016 (430) stainless steel, and observed that the Austenitic 1.4404 steel showed a considerable Bauschinger effect (B.R.=0.81), while the ferritic 1.4016 showed a tendency towards isotropic hardening behaviour (B.R.=0.92). Olsson [11] conducted biaxial tests on the Austenitic 1.4301, Austenitic 1.4436 and Duplex 1.4462 stainless steels and determined their B.R. as being 0.75, 0.70 and 0.60 respectively. Following the same testing procedures, Gozzi [12] further determined the Bauschinger effect of the Austenitic 1.4318 stainless steel as B.R.=0.65. In light of the experimental results, the stainless steels show a pronounced Bauschinger effect and a gradual transition from elastic to plastic state in subsequent loadings.

2.2. At elevated temperatures

In this section, comparisons of reduction in elastic modulus, 0.2% proof yield strength, plastic hardening curves, thermal expansion and thermal properties associated with temperature development within the structures, i.e. heat transfer analysis, between carbon steel and various grades of stainless steel are presented.

2.2.1. Strength and sitffness reduction

The primary motivation behind exploring stainless steel behaviour in fire conditions comes from observations of its superior stiffness and strength at elevated temperatures in various material testing when compared with conventional carbon steel.

Figure 1 presents the reduction factors of initial Elastic Modulus ($k_{E,\theta} = E_\theta/E$) provided by EC 3 [13] for carbon steel and DMSSS [2] for stainless steels, which shows that stainless steels offer better stiffness retention capability at temperatures higher than approximately 200 ℃.

Different from carbon steel, the tensile test stress-strain behaviour of duplex and austenitic stainless steels show no clearly defined yield point, thus it is the 0.2% proof stress provided in the design standards for stainless steels [14] that is usually considered. For structural fire design, a higher value of strength at 2% of total strain ($\sigma_{2\%}$) has been adopted in EC 3 [13] for both carbon steel and stainless steels.

Figure 2 shows the 2% strength reduction factor ($k2, \theta = \sigma_{2\%,\theta}/\sigma_{0.2\%}$) for carbon steel, austenitic and duplex groups of stainless steels. The $4th$ edition of DMSSS [2] categorised various grades of stainless steels into five basic groups. At lower temperatures, the stainless steels have a reduction factor of $k2, \theta$ greater than 1.0 owing to the use of the 2% strain limit for fire design and the substantial strain hardening that stainless steels exhibit. The Austenitic III offers overall the best $k2, \theta$ amongst all stainless and carbon steels.
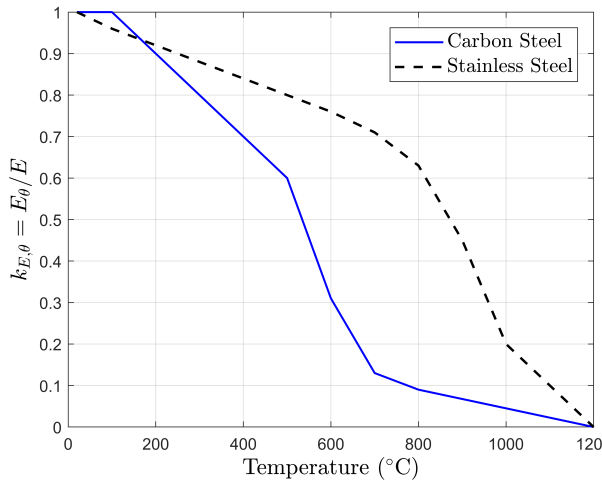

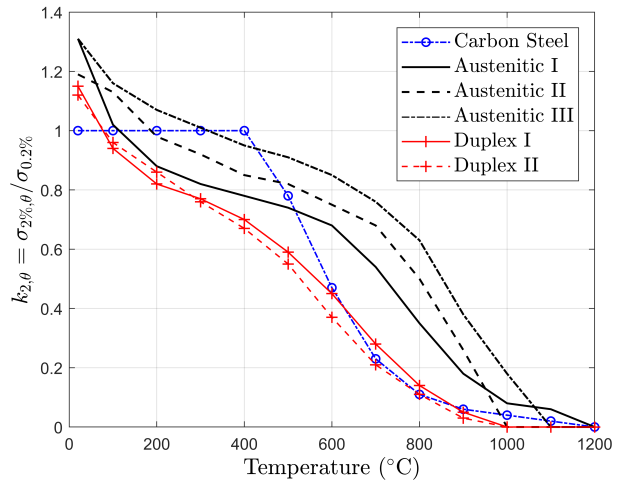**Figure 1:** $k_{E,\theta}$ at elevated temperature

Figure 2: $k_{2,\theta}$ at elevated temperature

4

2.2.2. Strain hardening relationships

The accuracy of the finite element model in analysing the behaviour of stainless steels is strongly dependent on the stress-strain constitutive relation employed, i.e. strain hardening functions. Unlike carbon steel displaying a saturation stress, stainless steels exhibit a substantial strain hardening effect. Therefore, a modified Ludwik strain hardening law [15] has been considered appropriate for stainless steels:

$$\sigma = \sigma_0 + k(\epsilon_{p,0} + \epsilon_p)^n \tag{2}$$

where σ_0 is the initial yield stress, and k and n are material parameters.

The parameter $\epsilon_{p,0}$ was introduced by the authors in this paper as the incipient plastic strain. Because stainless steels do not exhibit a distinct yielding point, in this study the initial yielding point (σ_0) is defined at the stress point where the plastic strain reaches 0.1% of the total strain, $\epsilon_{p,0} = 0.001\epsilon_{total}$.

The advantages of adopting the modified Ludwik law are twofold: firstly, by keeping the proportion of plastic strain to total strain (ϵ_p/ϵ) constant, the elastic range ($\sigma_{0_T}/\sigma_{0.2\%,T}$) of the stress-strain curves has been maintained uniform at elevated temperatures. This approach differs from traditionally adopting one proof strain, e.g. 0.01% as the yield point for all temperatures; secondly, the introduction of $\epsilon_{p,0}$, which was found to be of an order of magnitude of 10^{-6} for Austenitic III stainless steel and an order of magnitude 10^{-7} for Duplex II stainless steel, has circumvented the numerical instabilities caused by the original Ludwik law.

The hardening function parameters determined for the DMSSS Austenitic group III using least square fitting are summarised in Table 1. The Adj-R-square ratio was adopted as the fitting indicator. At each temperature level, the curve fitting value of σ_{0_T} is about 22% of the 0.2% proof strength ($\sigma_{0.2\%,_T}$). Table 2 presents the hardening function parameters determined for the DMSSS Duplex group II. A higher elastic region of the stress-strain curves is exhibited by the Duplex II when compared with the Austenitic III for a higher $\sigma_{0_T}/\sigma_{0.2\%,_T}$ ratio.

Table 1: Least Square Fitting Results for Hardening Law - Austenitic III

Temperature (℃)	σ_{0_T}	k_T	n_T	Adj-R-sq	$\sigma_{0_T}/\sigma_{0.2\%,_T}$
20	50.61	551.65	0.2003	0.99	0.23
100	43.08	484.22	0.1962	0.99	0.22
200	39.70	446.63	0.1964	0.99	0.22
300	37.27	426.00	0.1988	0.99	0.22
400	34.85	406.35	0.2021	0.99	0.22
500	33.40	389.78	0.2024	0.99	0.22
600	31.47	366.31	0.1995	0.99	0.22
700	28.56	311.30	0.1921	0.98	0.22
800	24.69	238.75	0.1734	0.97	0.22
900	13.40	153.97	0.1877	0.98	0.21
1000	7.26	91.26	0.2123	0.97	0.22

Table 2: Least Square Fitting Results for Hardening Law - Duplex II

Temperature (℃)	σ_{0_T}	k_T	n_T	Adj-R-sq	$\sigma_{0_T}/\sigma_{0.2\%,_T}$
20	171.16	1494.3	0.3673	0.98	0.38
100	140.30	1170.8	0.3544	0.98	0.38
200	116.60	951.3	0.3446	0.98	0.37
300	108.30	883.5	0.3446	0.98	0.37
400	99.96	808.7	0.3435	0.98	0.37
500	85.91	682.0	0.3343	0.98	0.36
600	66.18	514.1	0.3247	0.98	0.34
700	41.32	316.1	0.3029	0.98	0.31
800	2.93	22.5	0.2837	0.98	0.30
900	9.45	75.3	0.2756	0.98	0.25
1000	1.12	11.1	0.2631	0.98	0.25

Figure (3a) and Figure (3b) present the nominal stress-strain curves of Austenitic group III grades and Duplex group II grades based on DMSSS [2], respectively, together with their least square fitting curves. Overall, the Ludwik hardening law fits the nominal stress-strain curves to a satisfactory degree.

(a) Austenitic Group III

(b) Duplex Group II
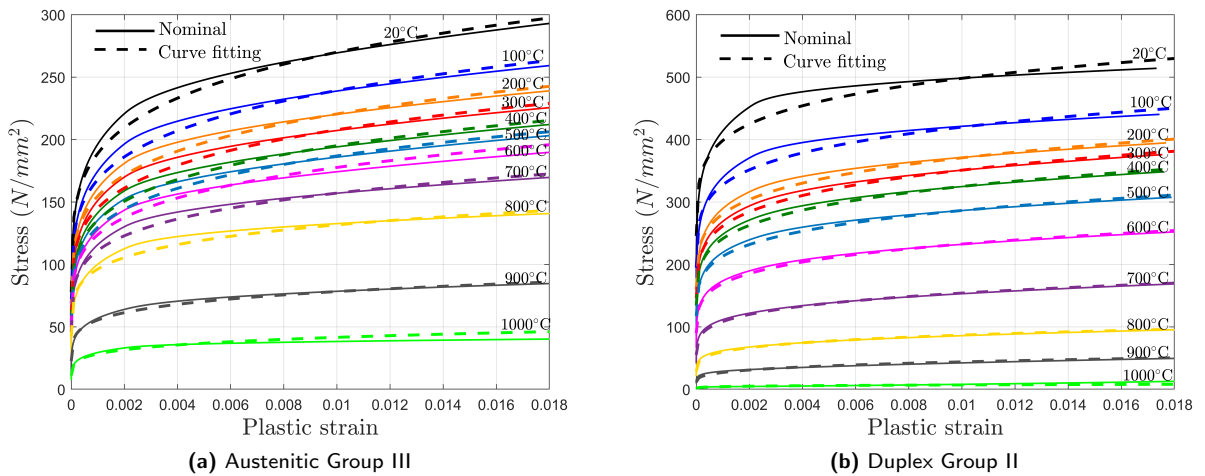
Figure 3: Stress strain curves at elevated temperatures, Nominal v.s. Curve fitting

2.2.3. Bauschinger effect

For various metals it has been observed that the Bauschinger effect is temperature dependent [16, 17, 18, 5]. Harvey et al. [17] investigated the evolution of the isotropic and kinematic hardening variables of the stainless steel 1.4307 (304L) stainless steel at elevated temperatures (20 °C, 200 °C, 600 °C, 800 °C and 1000 °C) using reverse yield experiments, and demonstrated the temperature-dependent nature of the Bauschinger effect. When investigating the material's kinematic hardening behaviour under cyclic loading at high temperatures, Ohno et al. [5] observed varying degrees of the Bauschinger effect and transient hardening at varying temperatures for the stainless steel 1.4301 (304).

2.2.4. Thermal expansion

The mean thermal expansion coefficients of typical stainless steels specified in DMSSS [2] are plotted in Figure 4, in the form of thermal elongation, and they are compared with that of carbon steel specified in the EC 3 [13]. As shown in the figure, stainless steels exhibit higher thermal expansion than carbon steel with austenitic grades having the highest values.
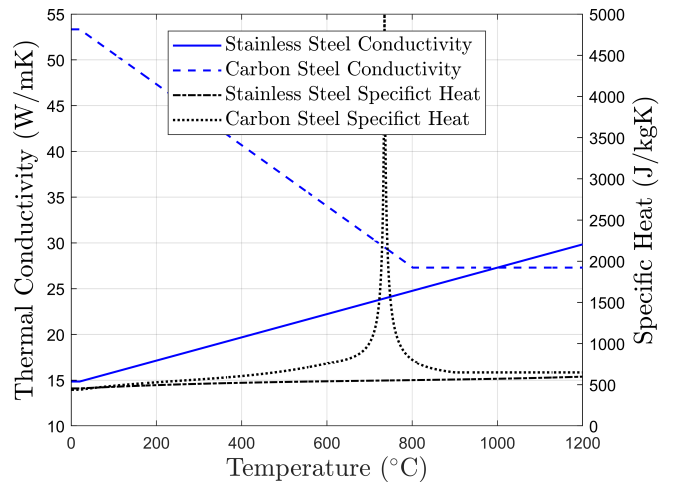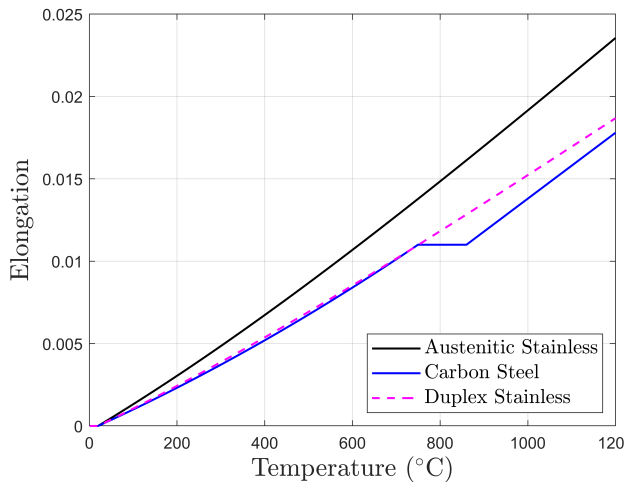

Figure 4: Thermal elongation at elevated temperature **Figure 5:** Conductivity and Specific heat at elevated temperature

2.2.5. Thermal properties

Stainless steels possess different thermal conductivity and specific heat when compared with carbon steel. The material property values provided by the DMSSS [2] for austenitic stainless steel and the EC 3 [13] values for carbon steel are presented and compared in Figure 5. On average, the specific heat of stainless steel is about $550 J/kgK$, as compared with approximately $600 J/kgK$ of carbon steel. One significant difference

is the austenitic stainless steel shows no phase change subjected to heating, whereas carbon steel exhibits a phase change in the region of 723 ℃, shown as the spike in the specific heat −temperature relationship.

The thermal conductivity of carbon steel reduces from $53W/mK$ at room temperature to $27W/mK$ at 800 ℃ and beyond. In contrast to carbon steel, the conductivity of austenitic stainless steel grow with rising temperature, increasing from 15W/mK at room temperature to about $30W/mK$ 1200 ℃. Overall, the stainless steel displays a lower thermal conductivity than carbon steel when temperature is below 1000 ℃. However, it is believed that their influence on the temperature development within structural I-sections is limited in building fires where the thermal environment is dominated by radiation heat transfer [19, 20]. The most significant difference is that stainless steels shows a lower emissivity of 0.4 than the 0.7 of carbon steel due to their polished surface according to EC 3 [13].

3. Uniaxial material model

The new material model of Zhou et al. [4] was presented as a multi-dimensional plasticity model. This section particularises it to a one-dimensional J_2 plasticity model, which was implemented as a uniaxial material model in OpenSEES. Firstly, a brief review of the new material model of Zhou et al. [4] is presented in the following.

The new material model is a combined isotropic and kinematic hardening rate independent plasticity model. It is a one-way coupled thermo-mechanical model in which temperature effects of external fire sources on the yield surfaces are integrated through the concept of a shrinking/expanding bounding surface, by exploiting the latitude of the two yield-surface models for kinematic hardening [21, 22], while the internal heat accumulation generated from plastic work resulted from large deformations during fire is neglected.

The Bauschinger effect is captured using the Bauschinger ratio (ϑ_T), defined as in Equation (1). The Bauschinger ratio is prescribed as an exponential function of accumulated plastic strain ($\overline{\varepsilon^p}$),

$$\vartheta_T = a_T * exp(-b_T * \overline{\varepsilon^p}) + c_T \tag{3}$$

where a_T, b_T, c_T are temperature dependent material coefficients.

The transient hardening behaviour is modelled by incorporating a second non-linear kinematic hardening variable, in which the reverse loading ratio (υ_T) parameter was introduced. The second kinematic hardening variable ($\dot{\boldsymbol{\beta_2}}$) is only activated when drastic change in the direction of plastic loading is detected and is defined as;

$$\dot{\boldsymbol{\beta_2}} = \dot{\upsilon}\sqrt{\frac{2}{3}}\dot{\overline{\beta_l}} * \boldsymbol{N} \tag{4}$$

where $\boldsymbol{N}$ is the unit deviatoric tensor normal to the yield surface. The $\overline{\beta_l}$ is a scalar that records the distance

the yield surface centre travelled during the last loading branch in the uniaxial stress direction, and can be obtained as follows:

$$\dot{\overline{\beta_l}} = V_{h_T}\sqrt{\frac{3}{2}\dot{\boldsymbol{\beta_n}} : \dot{\boldsymbol{\beta_n}}} \tag{5}$$

where $\dot{\boldsymbol{\beta}}_n$ is the rate of the (total) backstress tensor at the end of last loading branch prior to the start of reserve loading. The temperature dependent material parameter V_{h_T} is introduced to account for potential softening/hardening experienced during reverse loading. It can be obtained using experimental reverse stress strain data.

The reverse loading ratio υ_T is prescribed as an exponential decay function of the effective plastic strain of the new reloading branch, denoted $\overline{\varepsilon_l^p}$, as in Equation 6. The scalar $\overline{\varepsilon_l^p}$ accounts for the effective plastic strain accumulated during each loading branch, and will be reset to zero when reverse loading is detected.

$$\upsilon_T = 1.0 - exp(-V_{b_T} * \overline{\varepsilon_l^p}) \tag{6}$$

where V_{b_T} is the temperature dependent material coefficient, which can be obtained using experimental results of reverse stress-strain curves.

The new model solving the thermo-mechanical behaviour of a material using two sequential steps, a thermal step followed by a mechanical step. At the thermal step, the sizes of the bounding and yield surfaces, the parameters in the hardening function and in the evolution functions of the Bauschinger ratio and the reverse loading ratio are all updated to the current temperature (T). The size of the bounding surface can be determined using the uniaxial hardening curves combined with von Mises yield criterion. The Bauschinger ratio decomposes the total hardening into the isotropic and the kinematic hardening part to update the size and the centre position of the yield surface to the current temperature.

At the mechanical step, the stress state is considered isothermal, hence the temperature dependence can be considered "frozen" during the stress analysis. The backward-Euler method is adopted for the stress integration at the mechanical step. More detailed information for the multi-dimensional model/algorithm can be found in Zhou et al. [4]. The total material parameters adopted for the new model are summarised as follows:

1. Elastic modulus, E_T.

2. Initial yield strength, σ_{0_T}.

3. Hardening function parameters.

4. Parameters of Bauschinger ratio (ϑ_T) evolution function as shown in Equation 3.

5. Parameters of Reverse loading ratio (υ_T) evolution function as shown in Equation 6.

The multi-dimensional model has been adapted into a one-dimensional uniaxial model, and the numer-

ical algorithm for the uniaxial model is provided in Appendix A. The uniaxial material models "Stainless01Thermal" for the duplex stainless steel and "Stainless02Thermal" for the austenitic stainless steel have been implemented in OpenSEES [6], using the material parameters presented in Table 2 and Table 1 respectively. The uniaxial material model "SteelEC02Thermal" has been implemented for the carbon steel, which adopts the Voce hardening law [23], shown in Equation 7 as the strain hardening function, which required two hardening function parameters v_T and δ_T.

$$\sigma_{y,T} = \sigma_{y_0,T} + v_T * (1 - exp(-\delta_T \overline{\varepsilon_p})) \tag{7}$$

where $\sigma_{y_0,T}$ is the initial yield stress (yielding stress of proportional limit) at temperature T, which can be calculated using reduction factor (k_p) prescribed by EC3 for carbon steel or determined through least square fitting the stress-strain curves. The parameter v_T and δ_T are both temperature dependant material constants.

4. Validation of the Material Model under Transient Loading during Heating and Cooling

The capability of the new material model in capturing the evolution of the Bauschinger effect and transient hardening has been validated at elevated temperatures for isothermal loading conditions in Zhou et al. [4]. In real fire, the structures experience simultaneous loading and temperature changes, similar to a transient (anisothermal) loading condition. In this section, the proposed material model is further validated for transient loading conditions. The experimental data obtained by Ohno et al.[5], who conducted a series of thermo-mechanical cyclic experiments on stainless steel 1.4301 (304) under both isothermal and anisothermal loading conditions, has been adopted for this validation.

4.1. Experimental model

In this section, a brief description of the experiments conducted by Ohno et al. [5] is provided. The testing was conducted using a solid $160mm$ long bar specimens with a gauge of $20mm$ long and of $10mm$ diameter, as illustrated schematically in Figure 6.

The isothermal thermo-mechanical experiments were carried out at temperature levels of 150 ℃, 350 ℃, 600 ℃, 850 ℃ and 1000 ℃. With a strain rate of $10^{-4}s^{-1}$ the specimen was first strained to a maximum tensile strain of 0.005 followed by compressively strained to a strain of -0.005 while the temperature was kept constant.

The transient thermo-mechanical experiments were performed for four temperature ranges of [Tmin,Tmax].

The Tmin is 150 ℃ for all the four ranges whereas the Tmax varies from 350 ℃, 600 ℃, 850 ℃ to 1000 ℃. Whilst being heated from Tmin to Tmax, the specimen was loaded in compression at a strain rate of $4.17^{-5}s^{-1}$ to a maximum compressive strain of -0.01. In the subsequent cooling from Tmax to Tmin, the specimen was subjected to tension at a strain rate of $8.33^{-5}s^{-1}$ until it reached the final strain of 0.0. Forced air-cooling apparatus was used to cool the specimens from Tmax to Tmin within a time span of 240 seconds.

For the validation of the proposed material model, the experimental stress-strain results of the very first loading loop of the cyclic tests were used in this study, thus the cyclic hardening effect was not considered.

4.2. Validation model

The cross section of the gauge was modelled using 4-node plane stress elements in Abaqus/CAE. The model was restrained in axial direction on one end, and is presented in Figure 6. The multi-dimensional material model of Zhou et al. [4] implemented in the Abaqus Umat subroutine was for testing the stainless steel 1.4301.
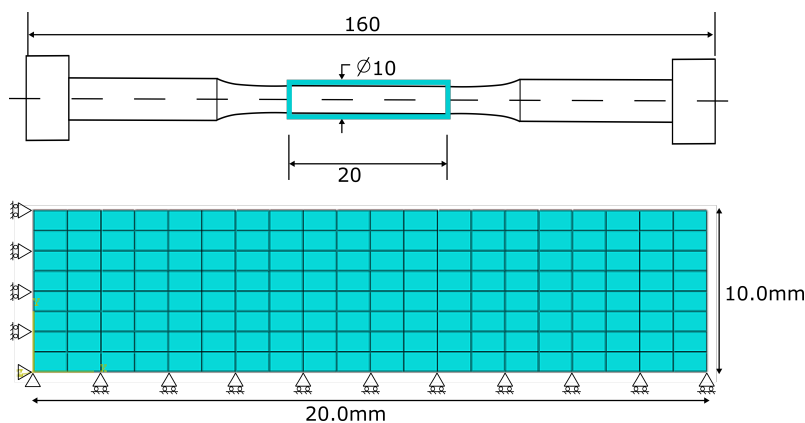

Figure 6: Thermo-mechanical test specimen (all dimensions in mm) [5]

The hardening function parameters were obtained by least square fitting the experimental tensile stress-strain curves from isothermal experiments using the modified Ludwik law of Equation (2). Table 3 summarises the hardening function parameters obtained.

Table 3: Least Square Fitting Results - stainless steel 1.4301

| Temperature | Hardening Function | | | Bauschinger Ratio Evolution Function | | | |
℃	v_T	δ_T	Adj-R-sq	a_T	b_T	c_T	Adj-R-sq
150	302.1	0.1675	0.977	0.38	1143	0.62	1.0
350	237.4	0.1729	0.984	0.28	1098	0.72	1.0
600	208.2	0.2144	0.998	0.25	1055	0.75	1.0
850	26.37	0.0748	0.975	0.26	974	0.74	1.0
1000	31.34	0.2569	0.939	0.37	1069	0.63	1.0

11

The Bauschinger ratio was determined based on the first loop of the stress-strain results of the cyclic isothermal experiments reported in [5]. For example the stress-strain result for 150 ℃ (Fig.8a) is reproduced in Figure 7 where the highest stress point (S11L) during monotonic loading and the lowest stress point (S11U) before the material enters the reversed hardening were identified and highlighted. The Bauschinger ratio was determined using Equation 8.
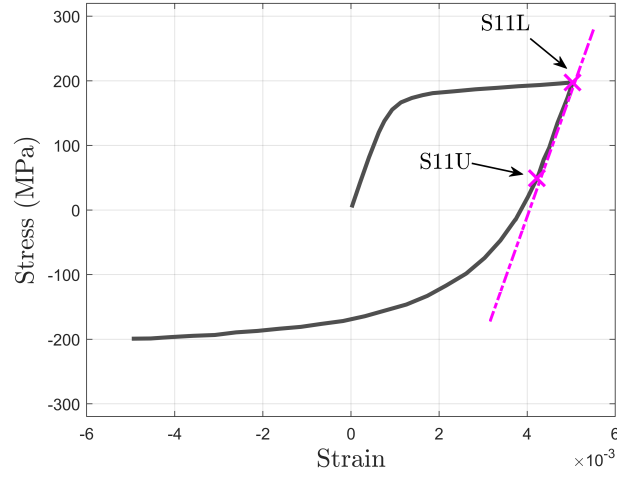

Figure 7: Calibration of the Bauschinger ratio

$$\kappa_{11} = \frac{S11L - S11U}{2}, \qquad \alpha_{11} = \frac{S11L + S11U}{2}, \qquad \vartheta = \frac{\kappa_{11}}{\kappa_{11} + \alpha_{11}} \tag{8}$$

where κ_{11} and α_{11} represents the amount of isotropic and kinematic hardening, respectively.

Table 4 summarises the Bauschinger ratios calibrated for the tested stainless steel 1.4301 at varying high temperatures based on the reported stress-strain results following the approach illustrated above. The Bauschinger ratios suggest that a substantial Bauschinger effect occurred in the tested stainless steel 1.4301 at elevated temperatures, similar to what was observed in [17].

Table 4: Bauschinger ratio calibration results, based on Fig.8 in [5]

Temperature	Bauschinger ratio	$\overline{\varepsilon^p}$
150 ℃	0.3756	0.0039
350 ℃	0.2766	0.0040
600 ℃	0.2463	0.0040
850 ℃	0.2797	0.0043
1000 ℃	0.3675	0.0047

The exponential function of Equation 3 was adopted in least square fitting to describe the Bauschinger ratio evolution as observed based on the stress-strain results of the first loading loop. The parameters for

the Bauschinger ratio evolution function are presented in Table 3.

4.3. Validation of isothermal thermo-mechanical experiments

Figure 8 compares the stress-strain development during the loading-reverse loading predicted by the new model of Zhou et al. [4] and the experimental data of the isothermal thermo-mechanical experiments at five varying temperatures. An overall good agreements have been observed, which suggests that the new material model is capable of capturing the Bauschinger effect and transient hardening behaviour very well under isothermal loading conditions. The model parameters of the new material model, namely the parameter V_b of the reverse loading ratio υ evolution function from Equation (6), and the parameter V_h of the second kinematic hardening term from Equation (5) were set to obtain the best possible overall curve fitting. The parameters used are summarised in Table 5.

Table 5: Model parameters, Isothermal experiments

Temperature	V_b	V_h
150 ℃	1100	1.80
350 ℃	1300	1.88
600 ℃	1600	1.86
850 ℃	2250	2.00
1000 ℃	2000	1.70

(a) T= 150°C

(b) T= 350°C

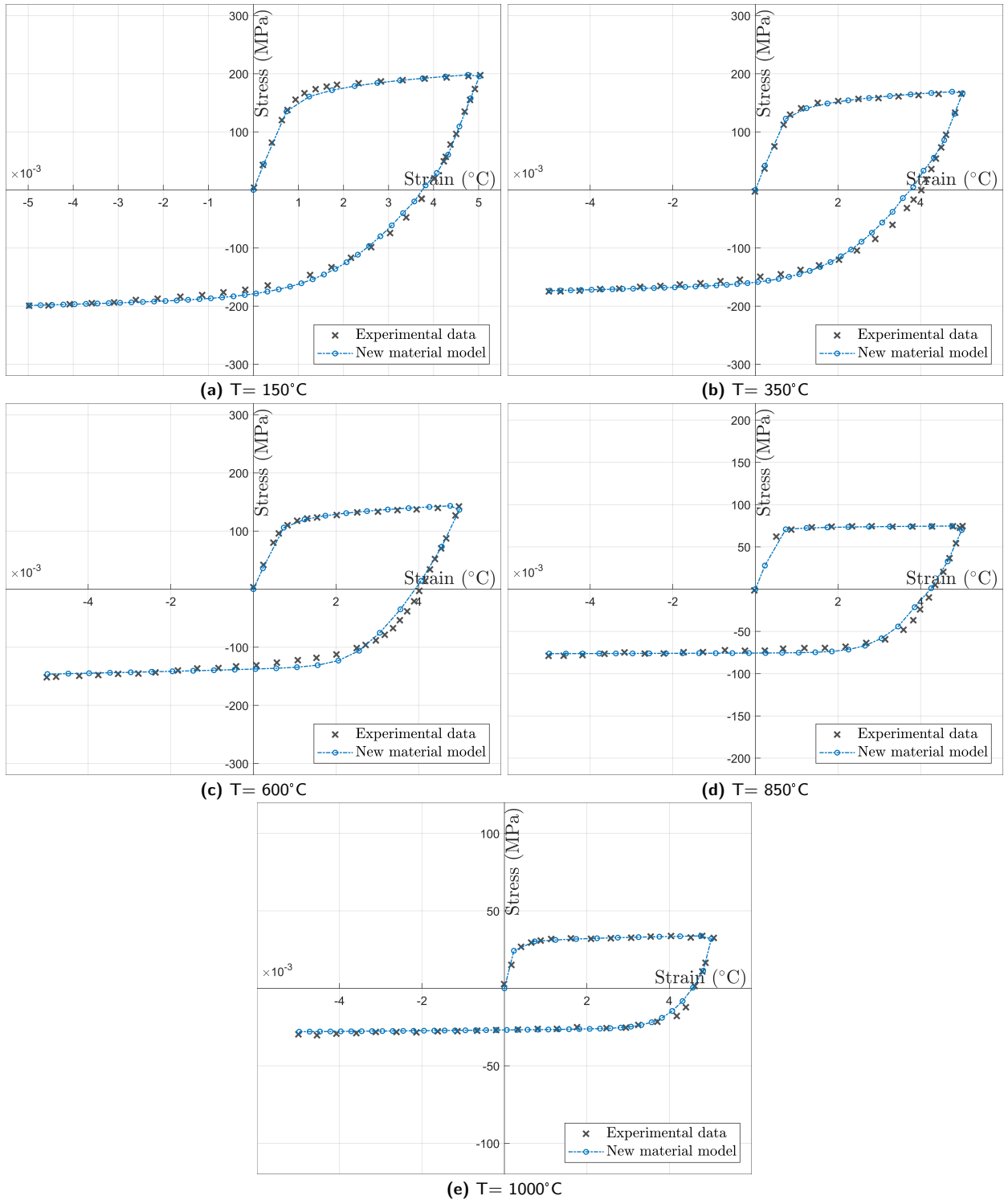**(c)** T= 600°C

(d) T= 850°C

(e) T= 1000°C

Figure 8: Stress strain curves comparison, Isothermal themo-mechanical experiments

4.4. Validation of transient (anisothermal) thermo-mechanical experiments

Figure 9 compares the stress-strain development during the loading-reverse loading predicted by the proposed material model and the experimental data of the four transient thermo-mechanical experiments. During initial compressive loading, small deviation between the predicted stresses and the experimental data were observed, particularity at higher temperatures. This is believed to be caused by the different constitutive behaviour in tensile and compressive loading of stainless steel material [24] because the hardening functions have been obtained based on the isothermal tensile stress-strain curves. The transient (anisothermal) state of loading could also be a source for the deviation. Nevertheless, it can be seen that the varying hardening modulus of the stress-strain curve during the heating has been captured well by the proposed material model.

For the reverse loading curve during cooling, the predictions of the proposed material model using the model parameters from Table 5 are in good agreement with the experimental data at 350 ℃ and 600 ℃.

For both 850 ℃ and 1000 ℃, higher values of V_h have to be adopted to achieve a satisfactory fit of the reverse stress-strain relationship. It's also noted that the material model parameter V_b ceased to be temperature dependent during cooling from 1000 ℃, a value of 800 was adopted for the entire cooling process. The model parameters used for at 850 ℃ and 1000 ℃ are summarised in Table 6.

The mechanical behaviour of steel materials is a phenomenological manifestation of their microstructure. The effect of very high temperatures on the microstructrue determines the material's mechanical behaviour when being cooled from the high temperature. Various experimental research [25, 26, 27, 28, 29, 30, 31, 32] have discovered that steel materials display different mechanical behaviour after being cooled from a critical maximum temperature (Tcr), i.e. little change in mechanical behaviour can be found if the materials are cooled down from a temperature that's lower than Tcr. Sufficiently high temperature exposure that causes phase changes in the mircostructure inevitably gives rise to different mechanical behaviour. It has been discovered that the transition of ferrite to austenite phase at high temperatures causes the change in the material's mechanical behaviour, which occurs above 650 ℃ in ultra-high strength steel [33] and around 800 ℃ in lean duplex stainless steel [32]. The transition of ferrite to martensite above 800 ℃ causes change in the mechanical behaviour in the ferritic stainless steel after being cooled from 800 ℃ [31]. Additionally, when exposed to a temperature higher than its Tcr, the material's post-fire mechanical behaviour becomes strongly influenced by the cooling rate [28, 31, 32].

The existing literature provide a sound explanation why different model parameters had to be deployed

15

in the material model of Zhou et al. [4] for the validation of the stress-strain relationship during cooling phase in the case of Tmax= 850 ˚C and 1000 ˚C. Figure (9c) and (9d) demonstrate the new material model offered good predictions of the reverse stress-strain behaviour for transient thermo-mechanical experiments. The material model parameter V_b and V_h adopted in the validation are summarised in Table 6. They were adopted to obtain the best possible overall fit of the reverse stress-strain curves.

Table 6: Model parameters, Transient experiments

Temperature	V_b	V_h
850 ˚C	2250	3.40
1000 ˚C	800	10.50

4.4.1. Comparison with isotropic hardening model

In Figure 9 the results of the new material model are also compared with the isotropic hardening model of Abaqus. The new combined isotropic-kinematic hardening material model works the same as the isotropic hardening model during the initial loading during heating. In reverse loading during cooling, the isotropic hardening model overestimates the stress response and cannot capture the transient hardening behaviour and variation in hardening modulus satisfactorily.

The material model presented has been shown to have the capability of describing accurately the experimentally observed phenomena, which traditional models are not capable to capture, e.g. the Bauschinger effect and the transient hardening and their consequences on the mechanical response to subsequent loadings during heating and during cooling. Comparisons and experimental results in general show good agreement with respect to initial and subsequent yield stress as well as stress-strain response, and the qualitative improvement compared to the simulations obtained using isotropic hardening model is quite evident.
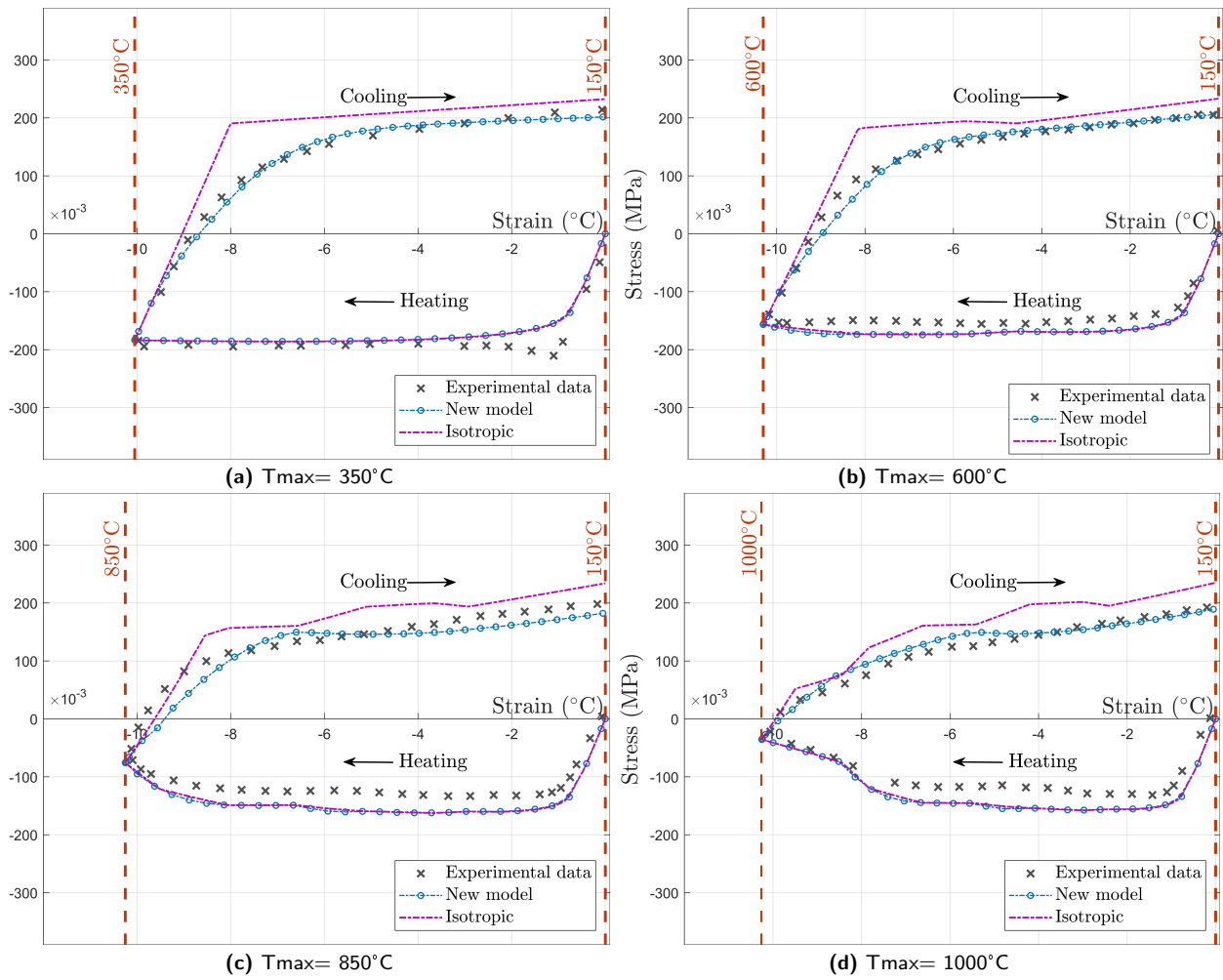
Figure 9: Stress strain curves comparison, Transient themo-mechanical experiments

17

5. Temperature Development in Stainless Steel I-Sections

In this section, the temperature development within structural stainless steel I-sections is investigated using heat transfer analysis conducted in OpenSEES. The impact of section factors (A/V), defined as the hearted perimeter of the exposed cross section divided by the total sectional area, is examined. A comparison study between structural stainless steels and structural carbon steel is performed.

5.1. Heat Transfer Model Validation

Validations of the FE model is performed by comparing the OpenSEES heat transfer results with the testing data and the Abaqus finite element results obtained by Gardner and Ng [34]. Recordings of the furnace temperature were adopted as the fire loading for the validation. The comparison results are presented in Figure 10, where a good agreement is generally observed. The sharp increase in the furnace temperature at around 850 ˚C for I120x64 and I160x82 has been well captured by the FE model.
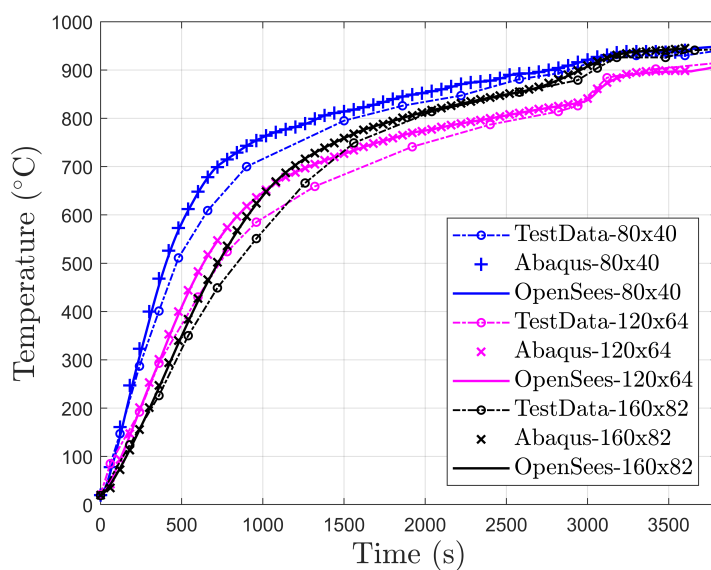
Figure 10: Temperature development within sections

5.2. Heat transfer parametric study

Temperature development within stainless steel I-sections is studied through a parametric study using the heat transfer model validated in the previous section. For steel I-sections subjected to high temperatures, radiation is the predominant heat transfer mode and conduction within the cross section is almost

instantaneous due to the high thermal conductivity. A comparison study of the temperature development within the carbon steel and stainless steel I-sections was carried out for 9 typical steel I-sections subjected to 4 sides heating. A summary of the dimensions of the 9 I-sections and their section factor (A/V) is presented in Table 7.

Table 7: Section dimensions and Section factors

Section	Depth (mm)	Width (mm)	Web t (mm)	Flange t (mm)	A/V (m^{-1})
UB914x305x289	926.6	307.7	19.5	32.0	83
UB762x267x197	769.8	268.0	15.6	25.4	104
UB914x419x388	921.0	420.5	21.4	36.6	71
UB610x305x238	635.8	311.4	18.4	31.4	82
UC305x305x198	339.9	314.5	19.1	31.4	76
UC254x254x73	254.1	254.6	8.6	14.2	166
UC356x406x634	474.6	424.0	47.6	77.0	32
UC356x406x393	419.0	407.0	30.6	49.2	48
UC356x406x235	381.0	394.8	18.4	30.2	78

The boundary conditions for the heat transfer analyses include convection and radiation. The I-sections were subjected to a 1 hour fire exposure defined by the Standard Fire Curve [35] on all 4 sides. In accordance with Eurocode 3 [13], the convection coefficient of $25W/m^2K$ was adopted for both carbon steel and stainless steel sections; the emissivity for radiation is adopted as 0.7 for carbon steel and 0.4 for stainless steel.

Figure 11 shows the temperature difference −time relationships at the bottom flange for each I-section. The temperature difference is determined as $Temp_{carbon} - Temp_{stainless}$ through the duration of the heating. $Temp_{carbon}$ is the temperature of the carbon steel while $Temp_{stainless}$ is the temperature of the stainless steel.

At the same time step, carbon steel I-sections experienced higher temperatures than stainless steel ones since only positive temperature differences were observed. A maximum temperature difference of 122 ˚C was observed at the bottom flange of section UC356x406x634, which is of the lowest A/V of $32m^{-1}$, at around 2400s. The section of the highest A/V of $166m^{-1}$ (UC254x254x73) experienced the lowest maximum temperature difference of 80 ˚C at about 600s. In general, it has been observed that higher A/V leads to a smaller magnitude and an earlier occurrence of the maximum temperature difference.

The same trend has also been observed at the mid-web of the I-sections, as shown in Figure 12. The slower temperature increase experienced in stainless steel is believed mainly attributed to its lower emissivity.
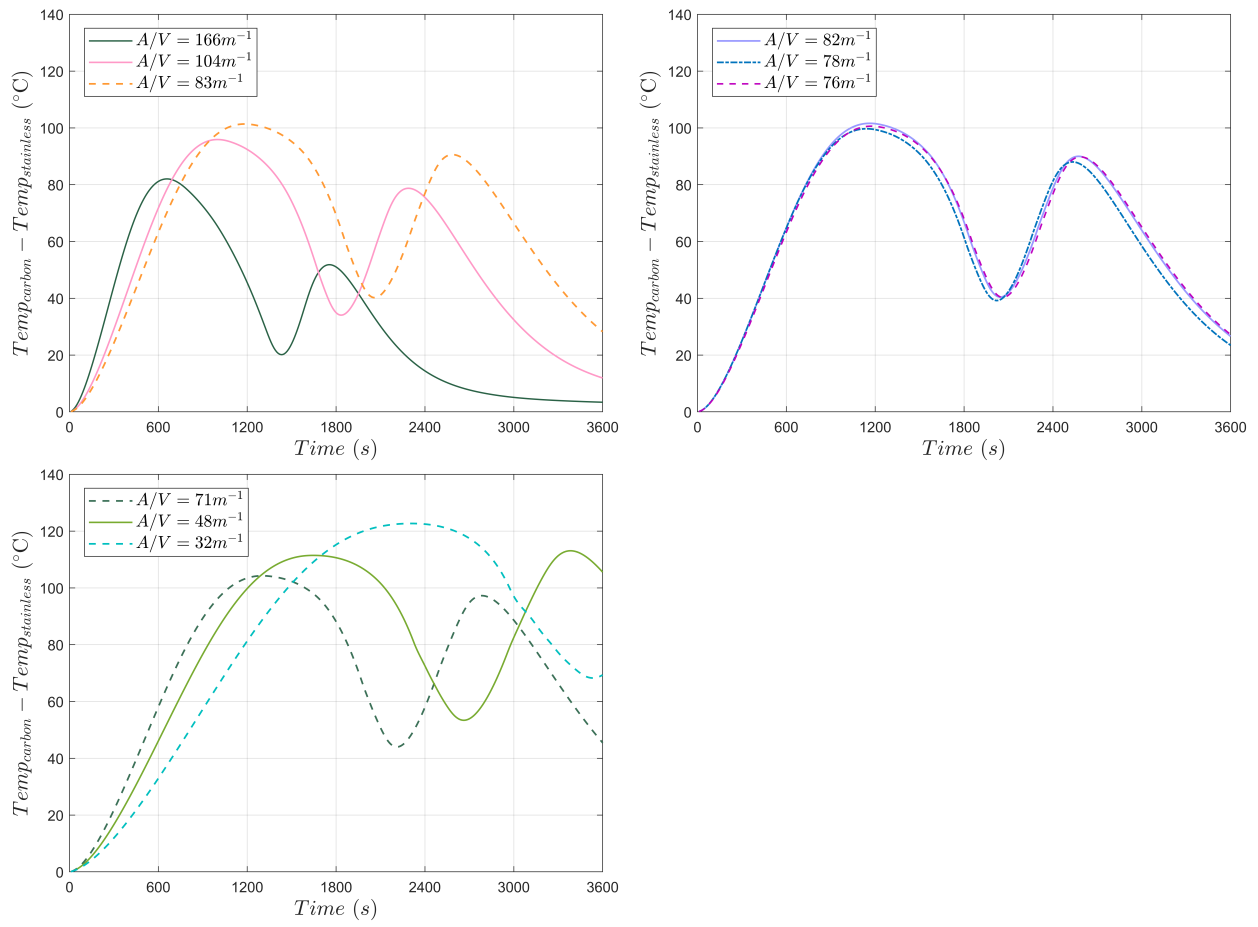
19

Figure 11: Temperature difference in bottom flange, 4 sides heated
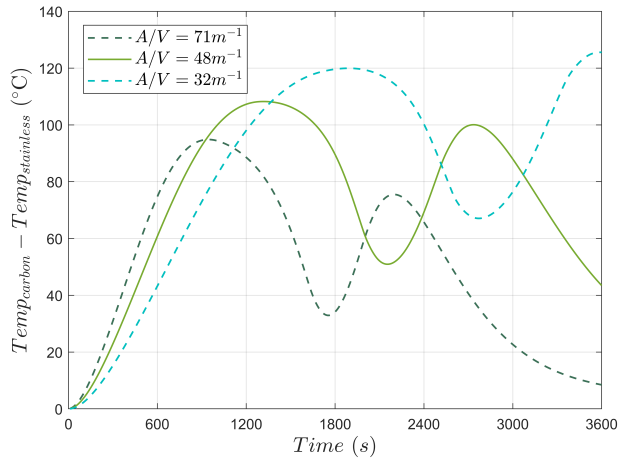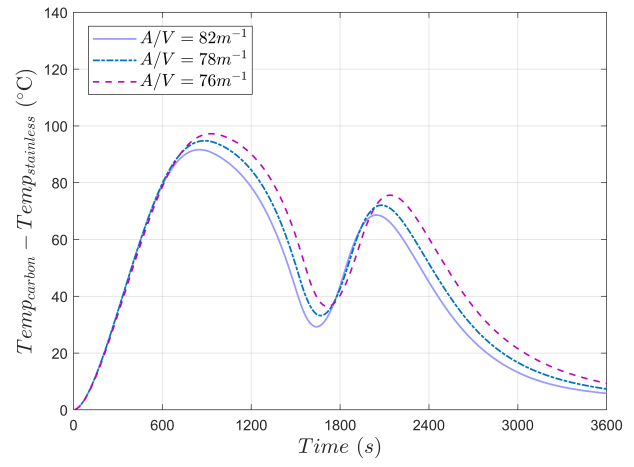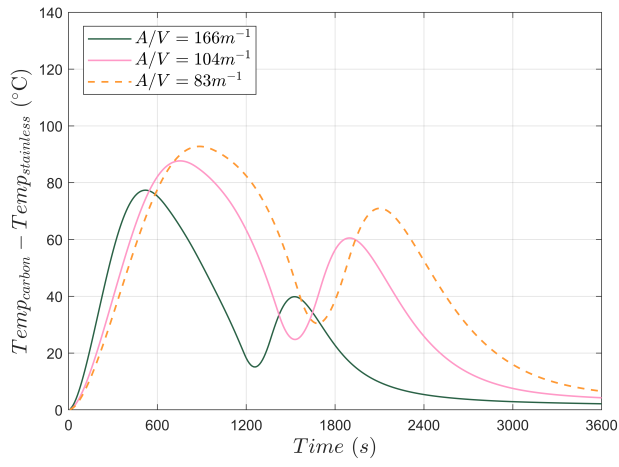
Figure 12: Temperature difference in web, 4 sides heated

6. Stainless Steel Structural Behaviour in Fire

Due to little available testing data for stainless steel structures at elevated temperatures, the FE models used in this study are the same that were already validated against existing testing data for carbon steel structures in fire.

6.1. Simply Supported Beams in Fire

6.1.1. FE Model Validation

Rubert and Schaumann [36] carried out a series tests on simply supported beams subjected to 4 sides heating. A point load was applied at the mid-span of the beam to generate varying initial load ratios (L.R.) ranging from 0.2 to 0.85.. The tested beams were of a length (L) = 1140 mm, with cross-section size IPE 80/ IPE 120, and made of St 37.2 Grade carbon steel.
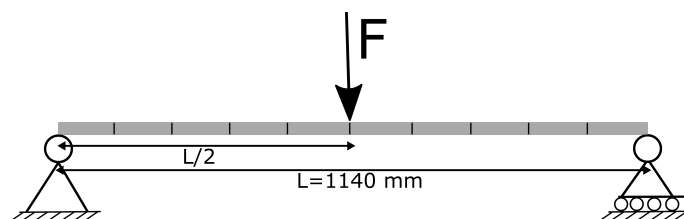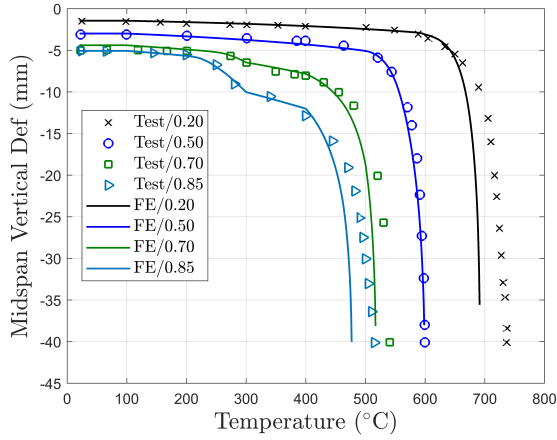

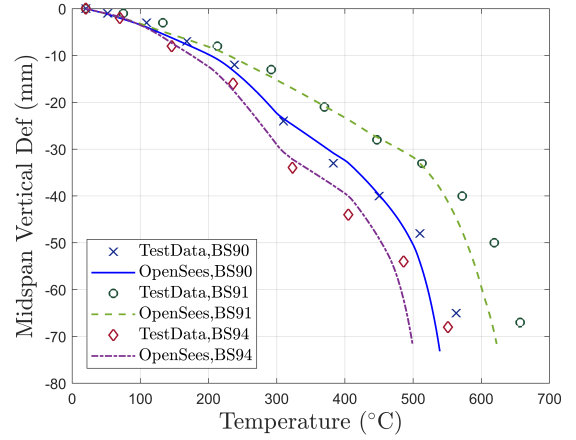**Figure 13:** Simply supported beam configuration

The simply supported beam was modelled in OpenSEES [6] using the Euler-Bernoulli beam theory based "DispBeamColumn2DThermal" element. As shown in Figure 13, the FE beam model is divided into 10 elements and is pinned at one end while free to move in the horizontal direction at the other end. The FE analysis accounted for both material and geometric non-linearities.

The L.R. was calculated as the the maximum bending moment applied on the simply supported beam over the plastic bending moment capacity of the beam at ambient temperature. The uniaxial material model SteelEC02Thermal was used for the St 37.2 grade carbon steel. The material parameters of the hardening functions applied in the SteelEC02Thermal for the validation were determined by least square fitting the stress-strain curves of the tested St 37.2 grade carbon steel in [36] using the Voce hardening law as in Equation 7. The determined and applied parameters are summarised in Table B.13.

The FE model was validated by comparing model predictions of the midspan deflection of the 4 sides heated beams with that of testing data. As shown in Figure 14a, a general good agreement has been observed between the testing data and the OpenSEES simulations.

22

(a) Four sides heating

(b) Three sides heating

Figure 14: Validation of simply supported beam model

A series tests of simply supported beams in fire were carried out by British Steel and documented in the Compendium of UK Standard Fire Test Data [37]. The testing data of three beams, BS90 (UB356x171x67), BS91 (356x171x67) and BS94 (IPE 360) were adopted for validation in this study. The beams were heated from three sides with the top being protected by a slab. There were no composite actions between the steel beam and the concrete slab. The FE model was further validated by comparing model predictions of the midspan deflection of the three sides heated beams with that of test data. As shown in Figure (14b), a general good agreement has been observed between the test data and the OpenSEES.

6.1.2. Comparison Study

Using the validated structural FE model, a comparison study was carried out to analyse the structural behaviour of simply supported stainless steel beams in fire. For this study, carbon steel S235, Austenitic 1.4571 (group III) and Duplex 1.4162 (group II) stainless steels have been selected. As discussed in Section 2.2.1, the Austenitic III shows the most promising stiffness and strength retention capability while the Duplex II shows an overall better stiffness and strength retention capability than the Duplex I. The lean duplex grade (Duplex 1.4162) was included in this study also because there has been a significant increase in its application in onshore building construction [38].

The room temperature values of the Young's modulus and the 0.2% proof strength ($\sigma_{0.2}$) for the three selected steels are summarised in Table 8. It is worth noting that DMSSS [2] proposes an identical Young's modulus value for the austenitic and duplex stainless steels, which is nearly the same to the carbon steel. The $\sigma_{0.2}$ of the austenitic steel is close to that of carbon steel, whereas the $\sigma_{0.2}$ of the duplex stainless

23

steel is almost double the $\sigma_{0.2}$ of the carbon steel. The uniaxial material model Stainless01Thermal and Stainless02Thermal were adopted for the Duplex 1.4162 and Austenitic 1.4571 stainless steel respectively. Where the material model parameters applied were obtained based on the least square fitting results of the nominal stress-strain relationships of stainless steels at elevated temperatures in DMSSS [2], as discussed in Section 2.2.2, which are presented in Table 1 and Table 2. For the carbon steel S235, the material model parameters determined using the least square fitting results of the EC 3 [13] stress-strain curves at elevated temperatures were applied in the SteelEC02Thermal, as summarised in Table B.14. Considering the main objective of this study is investigating the influence of stainless steel's non-linear stress-strain relationships and higher thermal expansion on its structural fire behaviour in comparison to carbon steel, the Bauschinger effect is therefore not included in this study. A Bauschinger ratio of 1.0 was adopted for all the materials.

Table 8: Material properties

Material Property	S235	Austenitic	Duplex
Young's modulus (GPa)	210	200	200
$\sigma_{0.2\%}$ (MPa)	235	220	450

In this study, four series of comparison analyses were performed. The applied load, initial deflection and initial L.R. of each beam for each series are summarised in Table 9. In each series, the magnitude of the applied load was kept constant for the three beams of different steel materials. Comparable initial midspan deflections were attained due to the similar Young's modulus of the carbon steel and the stainless steels, with slightly higher deflection observed in stainless steels. In each series, the initial L.R.s of duplex steel beams were almost half of the carbon steel and austenitic stainless steel beams because of its higher $\sigma_{0.2}$ value. In the Series 4, a significantly higher initial deflection is observed for the austenitic stainless steel beam, indicating the tangent modulus is already considerably lower than the initial elastic modulus at the start of the fire.

Table 9: Comparison study series, Simply supported beams

Series	Applied Load	Initial Deflection (mm)			L.R.		
No.	(kN)	S235	Austenitic	Duplex	S235	Austenitic	Duplex
1	3.71	0.70	0.75	0.75	0.20	0.21	0.10
2	9.27	1.8	1.9	1.9	0.50	0.53	0.26
3	12.98	2.5	3.1	2.6	0.70	0.75	0.37
4	15.77	3.0	4.9	3.2	0.85	0.95	0.44

The midspan deflection vs. temperature curves are presented in Figure 15. In the first series, the deflection of the carbon steel beam started to increase rapidly at around 650 ℃ and the run-away mechanism

occurred at about 750 ˚C. Identical deflections were observed for the austenitic and duplex beams until near the occurrence of the run-away mechanism, which was at around 750 ˚C for the duplex and at around 900 ˚C for the austenitic steel. Based on the deflection results of the first series, the two stainless steels exhibit superior behaviour to that of carbon steel with the run-away mechanism occurring at the highest temperature for the Austenitic 1.4571 beam. The mechanical stress-strain results of the Series 1 are presented in Figure 16a. The carbon steel showed a linear stress-strain relationship in their results, whereas noticeable strain hardening was observed in the stainless steel beams. It's worth noting that thermal strain does not contribute to material yielding in simply supported beams.
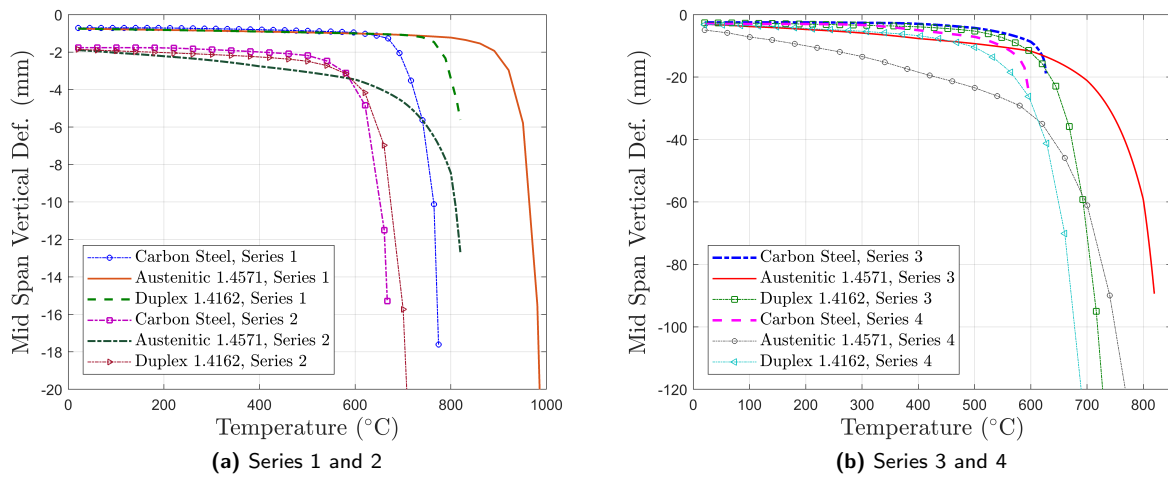

(a) Series 1 and 2
(b) Series 3 and 4

Figure 15: Deflection comparisons, simply supported beam

Figure 15a shows that for the second series, the deflection of austenitic beam develops faster than the other two beams because the Austenitic 1.4571 steel approaches the non-linear region faster. The deflection vs. temperature curve suggests that with the initial L.R. =0.53, the Austenitic 1.4571 experienced a faster and higher reduction in its tangent modulus. The run-away mechanism was still evident at the highest temperature for the austenitic beam, at around 800 ˚C. The run-away mechanism for the carbon steel beam and for the Duplex 1.4162 beam initiated at a similar temperature, around 600 ˚C. As shown in Figure 16b, substantial amount of strain hardening was observed for the stainless steel beams.

For the third series, Figure 15b shows that with L.R. =0.75, higher initial deflection and faster deflection development is observed for the austenitic beam. This is due to faster reduction in the tangent modulus as the material approaches plastic state. The run-away mechanism occurred at about 610 ˚for the carbon steel beam, at around 700 ˚C for the duplex beam and at around 800 ˚C for the austenitic beam.

For the fourth series, starting with similar initial deflections, the carbon steel beam displayed a slower

deflection development than the duplex beam until the run-away occurred at around 550 ℃. The deflection of the Duplex 1.4162 started to increase quickly at around 500 ℃ and reached 114 mm (L/10) at about 690 ℃. Due to the high initial L.R., austenitic beam was already in the plastic state at the start of the heating, resulting in significant reduction in the tangent modulus. This was manifested as higher initial deflection and notably faster deflection rate in the austenitic beam than the other two steel beams. However, due to its superior stiffness retention, the austenitic beam reached the large deflection of 114 mm (L/10) later at about 750 ℃. Figure 16c and 16d show that in Series 3 and 4, substantial strain hardening was able to develop in the simply supported stainless steel beams while none was observed for the simply supported carbon steel beams.
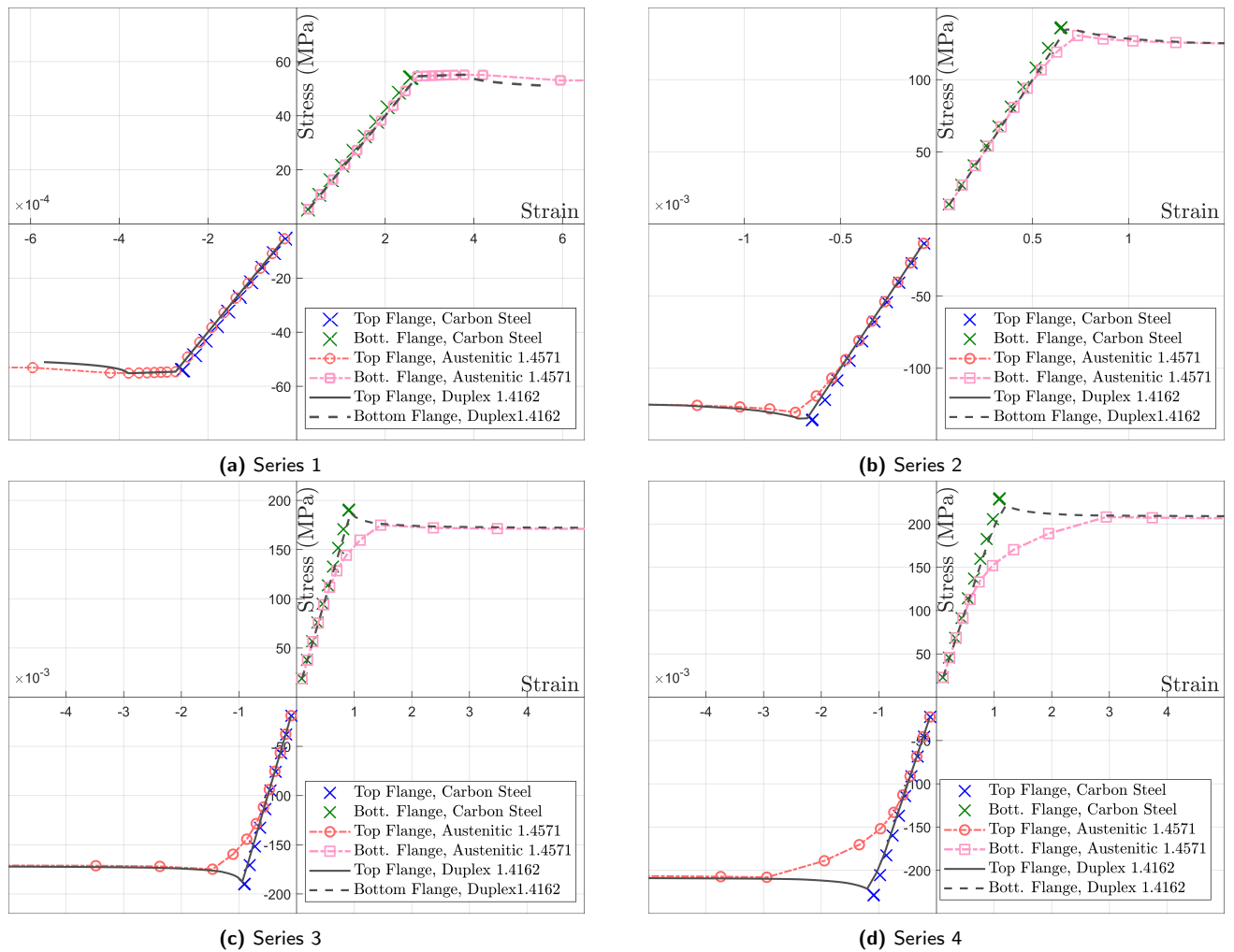

(a) Series 1

(b) Series 2

(c) Series 3

(d) Series 4

Figure 16: Stress strain development, simply supported beam

26

6.1.3. Discussions

The deflection results suggest that the initiation of the run-away mechanism for simply supported beams in fire is primarily determined by the material's stiffness degradation and the initial load ratio. At the lowest L.R., the run-away mechanism occurs when the stiffness of the material starts to deteriorate rapidly, at around 500 ˚C for the carbon steel and 800 ˚C for the stainless steel. For carbon steel, the elastic modulus retention capability at elevated temperatures is a good indication to the occurrence of the run-away mechanism in simply supported beams. For simply supported stainless steel beams with higher initial L.R., the retention factor $(k_{E,\theta})$ cannot indicate well the occurrence of the run-away mechanism, because the plastic hardening developed in the material gives rise to significant reduction in the tangent modulus.

The comparison study between the simply supported stainless steel and the carbon steel beams shows that the Austenitic 1.4571 beam exhibits the best behaviour based on the judgement of midspan deflection development. This is as expected because of its overall superior stiffness and strength retention capability, as shown in Figure 1 and Figure 2. However, at higher L.R.s, the early reduction in the tangent modulus of the stainless steel results in faster deflection development rate.

The stress-strain plots show similar behaviour for the four different L.R.s, as seen in Figure 16. The most significant difference observed between the simply supported carbon steel and stainless steel beams is that the plastic state occurred at a lower strain level, hence lower L.R.s, in the austenitic stainless steel beams. This is caused by the significantly shorter linear elastic stress-strain range of the stainless steels..

The FE results of the carbon steel stress strain response did not observe any plastic strain development. However, it should be noted that the FE analysis terminated in the carbon steel beams quickly after its deflection vs. temperature curve started approaching vertical, as the static analysis could not cope with the sudden substantial loss of the structural stiffness. The elastic modulus of carbon steel rapidly reduces from 60% of its room temperature value at 500 ˚C to about only 30% at 600 ˚C. The deflection results were still in the small deflection regime when the FE analysis terminated hence plastic hardening was not experienced in the numerical model. Plastic strain would be experienced in real life beams during the development of large deflections following the occurrence of the run-away mechanism.

6.2. Plane Frame Structures in Fire

6.2.1. FE Model Validation

Unlike simply supported beams, thermal expansion induced compression dominates beam behaviour in real structures where there exist end restraints provided by the surrounding structure. Consequently, the performance of stainless steel frame structures in fire will be determined by two competing factors: superior stiffness retention and high thermal expansion.

The study of stainless steel frames was carried out using finite element analysis with the FE model validated against the testing data of the EHR3 carbon steel frame tests performed by Rubert and Schaumann [36]. The configuration of the EHR3 frame is illustrated in Figure 17. The beam and the column was divided into 16 elements respectively in the FEA model of the frame, which is also shown as schematically in Figure 17. All members were uniformly heated during the test. The frame beam was pinned at right end while the column was pinned at the bottom. The lateral torsional displacement and the out-of-plane deformation were prevented by using stiffeners, hence the 2D plane frame model could be used for this study.

Validation of the FE model was carried out by comparing the temperature-deformation history, (deflection U2 and V4 as illustrated in Figure 17) predicted by the FE model with that from experimental results. The material model parameters in Table B.13 for the carbon steel St37 were used. A general good agreement can be observed for the results presented in Figure 18.

The predicted critical temperatures, defined as the maximum temperature anywhere on the frame at which deformations increased in an uncontrollable fashion and corresponding to the last converged solution from the program are also provided in Table 10. These compare very well with those reported from tests [36].
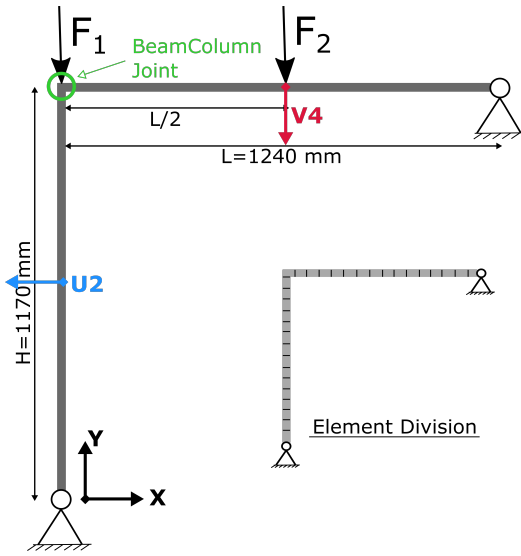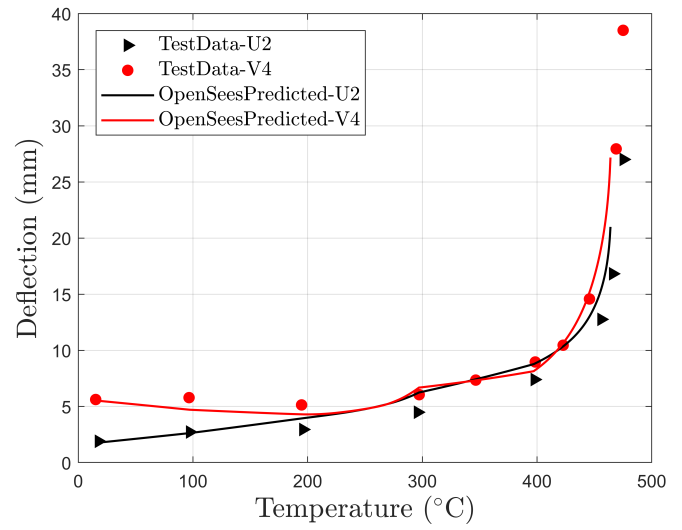
Figure 17: EHR3 Frame configuration

Figure 18: EHR3 Frame deflection comparison

Table 10: Test parameters used in Validation

Type	l (mm)	h (mm)	σ_y (N/mm^2)	F1 (kN)	F2 (kN)	Critical Temp Tested (°C)	Critical Temp Predicted (°C)
EHR3	1240	1170	382	112	28	475	467

6.2.2. Comparison study

Using the validated FE model, the structural behaviour of stainless steel frames in fire was investigated and compared with that of EC 3 carbon steel frame. Similar to the comparison study of the simply supported beams, the carbon steel S235, Austenitic 1.4571 (group III) and Duplex 1.4162 (group II) have been adopted for this frame comparison study. The same material models used in the study of the simply supported beam in Section 6.1.2, namely Stainless01Thermal, Stainless02Thermal, SteelEC02Thermal were adopted for the analysis of the frame structures. A Bauschinger ratio of 1.0 was adopted for all the steel models.

Three series of load ratios (L.R.s) of the frames were investigated, as summarised in Table 11. The L.R. for the beam was calculated as the maximum bending moment applied on the beam to the plastic bending moment capacity of the beam at ambient temperature. The L.R. for the column was calculated as the maximum axial force on the column over the axial capacity of the column at ambient temperature. Lower load ratios were adopted for the columns as columns behave less robustly than beams in fire due to their high axial compressive loading, possible buckling failure and lack of secondary load carrying mechanisms such as catenary action. The influence of the L.R. on the behaviour of frames of the three materials at elevated temperatures were examined.

29

Table 11: Comparison study series, EHR3 frame

Series No.	L.R. in Beam	L.R. in Column
1	0.15	0.075
2	0.30	0.15
3	0.60	0.30

Since there were no restraints at the beam-column joint, the beam could expand to the left whilst the column could expand upwards during heating. As a result, the V4 deflection of the beam moved upwards in the positive direction of the global Y axis in the beginning, whereas the U2 displacement of the column moved leftwards in the negative direction of the global X axis.

Figure 19 compares the midspan deflection results of the frame beam (V4) of the three series. During heating, the V4 increased initially as a result of the thermal expansion in the column. As the stiffness of the column reduced at increasing temperatures, a rapid drop in the V4 was observed, indicating the collapse of the column.

In the Series 1 to 3, the V4 of the Austenitic 1.4571 steel showed the highest upward movement since the austenitic stainless steel possessing the highest thermal elongation. In the Series 3, the upward behaviour was not observed for the V4 deflection of the Duplex 1.4162 steel, suggesting the duplex column was already in the plastic state when L.R. reached the value of 0.30.

The column collapse occurred at the highest temperature for the Austenitic 1.4571 frame, however the degree of this advantage diminished as the L.R. increased. When the column achieved L.R.=0.075, the Austenitic 1.4571 steel postponed the collapse by approximately 280 ˚C in comparison to the carbon steel. This value dropped to 180 ˚C when the column L.R. increased to 0.30.

With similar initial deflection (Duplex 1.4162 in the Series 1 compared with carbon steel and Austenitic 1.4571 in the Series 2; Series 2 Duplex 1.4162 compared with the other two materials in the Series 3), the frame collapse occurred at higher temperatures for the Duplex 1.4162 than for the carbon S235, but the temperatures were still lower than that of the Austenitic 1.4571 steel. Within each series, the same initial L.R.s were shared by the frame beams and columns of the three different steel materials. For the Series 1, the Duplex 1.4162 frame collapsed at a temperature about 10 ˚C higher than that of the carbon S235 and 210 ˚C lower than that of the Austenitic 1.4571 steel. For the Series 2 and 3, the Duplex 1.4162 frame collapsed at the lowest temperature among the three materials.
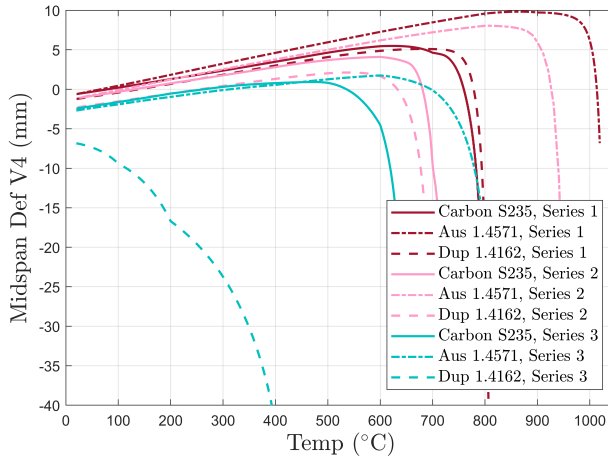
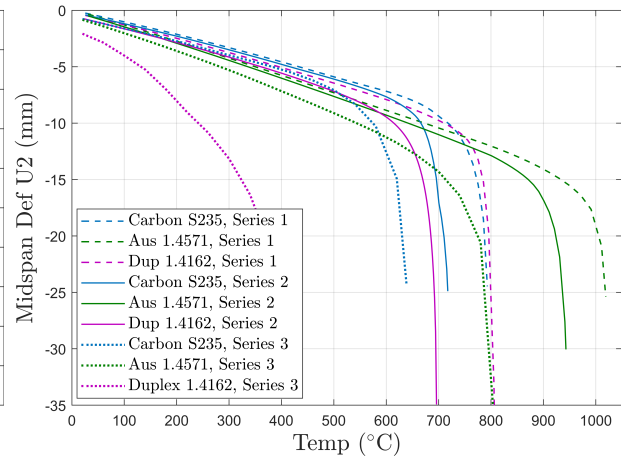**Figure 19:** Midspan deflection V4, Frame beam

Figure 20: Midspan deflection U2, Frame column

The midspan deflection results of the frame column (U2) are presented and compared in Figure 20. During heating, the U2 displayed a linear increase along the negative direction of the global X axis because of the beam expansion in that direction, until the large deflection mode occurred as a result of the column collapse.

The deflection results of the frame beam (V4) and of the frame column (U2) showed a clear advantage of the Austenitic 1.4571 steel in delaying the collapse of the frame structure. For the duplex 1.4162, the superior behaviour when compared with the carbon steel was only evident in the Series 1. The degree of the advantage offered by the two stainless steel grades diminishes as the L.R. increases. As seen from the previous comparison study of simply supported beams, stainless steels enter the plastic domain at lower strains than carbon steel because of their shorter elasticity range. The results of the Series 3 showed that the Duplex 1.4162 frame rapidly developed into the collapse mode since the column, with an initial L.R.=0.30, was already in the plastic state at the start of the fire. The comparison results demonstrate that the initial plasticity of stainless steel columns are detrimental to the structural fire performance of stainless steel frames.

Figure 21 presents the stress strain development at the beam-column joint of the Series 1 during the heating, in the beam and in the column respectively. The stress at the bottom of the beam cross section and the right hand side (RHS) of the column section are in negative while at the top the beam cross section and the left hand side (LHS) of the column section are in positive as seen in the figure. The stress strain results of Series 1 (which is of the lowest L.R.s) showed that substantial plastic hardening was already developed during the fire. The austenitic beam-column joint experienced the highest plastic hardening for this case. The strain reversals occurred at the lowest strain value for the duplex column at the joint.
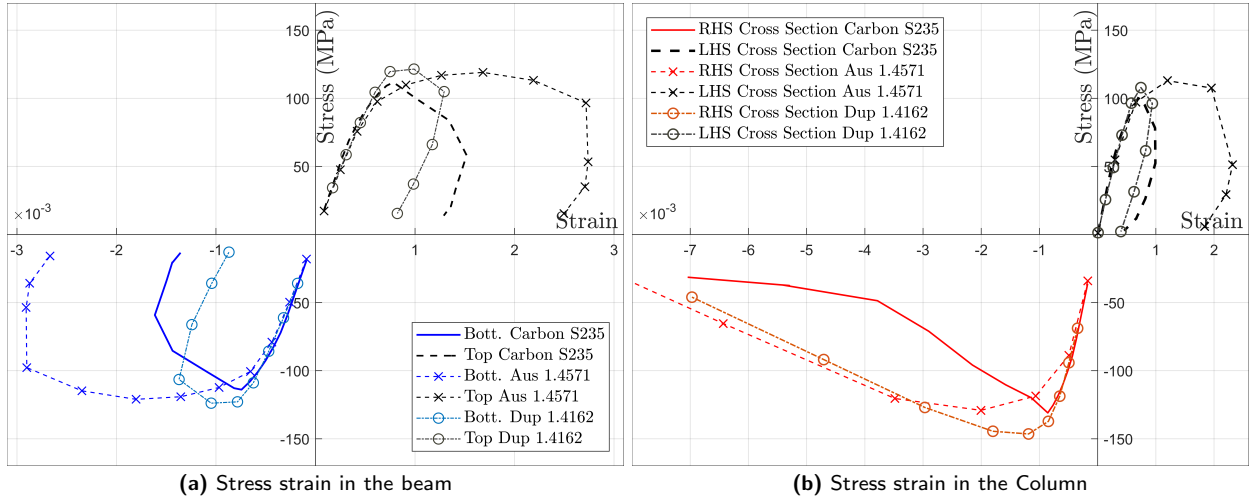
31

(a) Stress strain in the beam   **(b)** Stress strain in the Column

Figure 21: Stress strain at the beam-column joint

6.2.3. Effect of axial restraints

The EHR3 frame represents a single frame structure where the beam-column joint is free to move without any external axial restraints during fire. In reality, during a fire, there exist axial restraints on the beam-column joints provided by the surrounding cooler structure. The effect of external axial restraints are of particular research interest for stainless steel structural performance in fire because stainless steels exhibit higher thermal elongations when compared to carbon steel, as shown in Figure 4.

In this section, the effect of external axial restraints on the structural behaviour of the frame column and beam was studied by applying varying degrees of axial restraints to them at the beam-column joint, as illustrated in Figure 22. The axial restraints were modelled using elastic spring elements. Three levels of axial restraints were investigated, which are $0.05K_\beta$, $0.15K_\beta$ and $0.30K_\beta$, where K_β is the axial stiffness of the structural component (frame column or beam) at ambient temperature. The restraint stiffness was considered constant during the fire. The L.R.s of the Series 2 and 3 in the previous comparison study was selected for this parametric study. For the Series 2, the L.R. of beam=0.30 and L.R. of column=0.15; for the Series 3, the L.R. of beam=0.60 and L.R. of column=0.30.
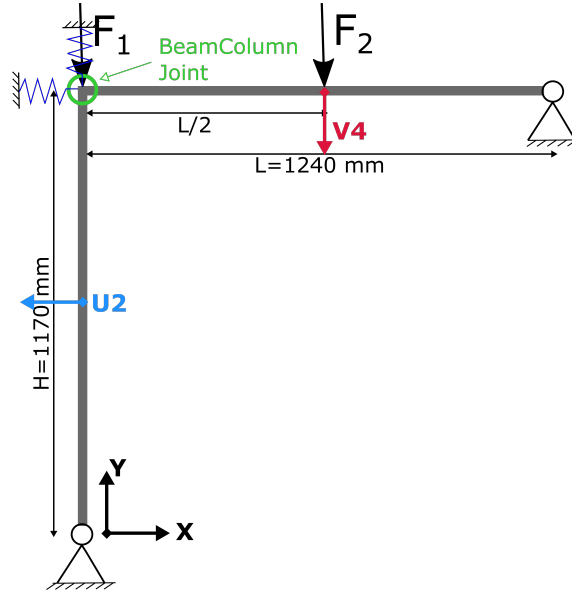
Figure 22: EHR3 frame with external axial restraints applied

Figure 23 compares the midspan deflection (V4) development of the frame beam without any external axial restraints at the beam-column joint and with axial restraints of varying degrees of stiffness, under the L.R.=0.30. It shows that as the restraint stiffness increases, the magnitude of the initial upward movement resulting from column expansion reduces, also the temperature at which the beam begins to displace downward decreases. When there were no external restraints ($k_\beta = 0.0$), the run-away mechanism was observed at around 910 ˚C for the austenitic steel beam, at about 700 ˚C for the carbon steel beam and at about 680 ˚C for the duplex steel beam. These temperature values correspond to the collapse temperatures of the columns (L.R.=0.15), as shown in Figure 24. The initiation of the column collapse is considered to coincide with the reversal of the direction of vertical displacement from positive to negative when plotted against temperature.

Figure 24 shows that the introduction of external restraints of $k_\beta = 0.05$ decreases the collapse temperature of the columns: the turning point of the disp vs. temp curve of the austenitic column reduced from around 910 ˚C to about 880 ˚C, from 680 ˚C to around 640 ˚C for the carbon steel beam and from 660 ˚C to around 560 ˚C for the duplex steel beam. This behaviour is expected as the restrained thermal expansion increases the load on the columns. The inclusion of external restraints also induces gradual development of V4 into the large displacement regime, in contrast to the abrupt run-away point observed for the unrestrained beams. Due to the external restraints, instead of running away, the beam goes into catenary action in the large displacement regime.

The increase of restraint stiffness level has little impact on the turning point of the column vertical disp vs. temp curve. The same behaviour is seen in the results of beam midspan deflection (V4), shown in Figure 23, as the beams of the same material with varying levels of restraint stiffness entered large deflection regime at similar temperatures. The three restrained austenitic beams reached a large deflection of 70 mm (L/18) at aound 900 °C; the restrained carbon beams reached 60 mm (L/21) at about 720 °C and the restrained duplex beams all reached 60 mm (L/21) at about 680 °C.
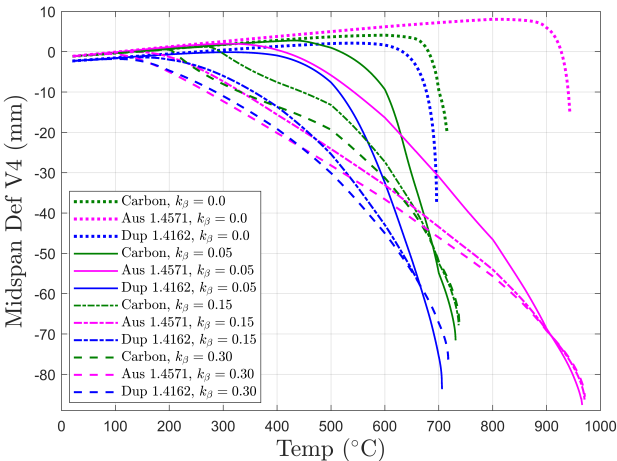

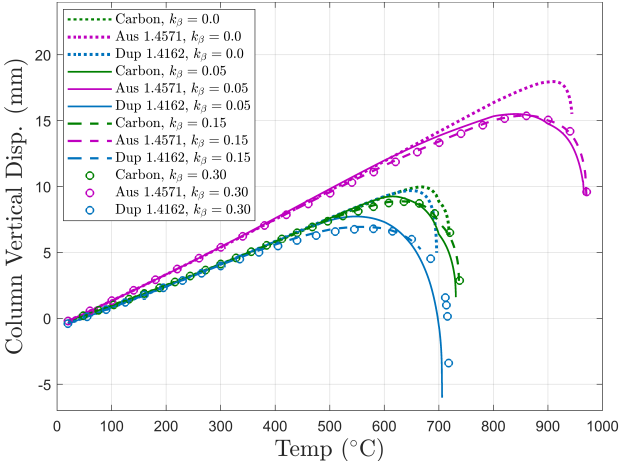**Figure 23:** Beam midspan def vs. temp, Beam L.R.=0.30

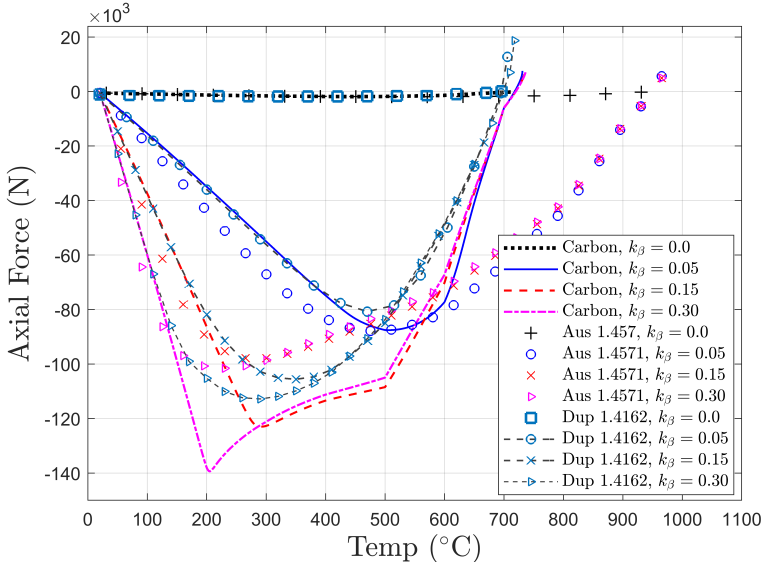**Figure 24:** Column vertical disp vs. temp, Column L.R.=0.15

Figure 25: Beam axial force vs. temp., Beam L.R.=0.30

Figure 25 compares the axial force in the frame beam with varying degrees of axial restraints. The higher axial restraint stiffness is the higher the maximum compressive force will be. With the same degree of axial

34

restraint stiffness, the compression resulted from the restrained thermal expansion increased at the fastest rate for the Austenitic 1.4571 beam due to its highest thermal elongation.

The maxima of the axial force vs. temp curve occurs when the beam cross-section reaches its axial capacity. At the stiffness level of $0.15K_\beta$ and $0.30K_\beta$, the carbon steel beam showed significantly higher maximum compression than the other two stainless steel beams, because the carbon steel beam possesses higher bending resistance capacity in the lower temperature range. When compared with the stainless steels, carbon steel exhibits superior stiffness retention capability at temperatures lower than 200 ℃, as seen in Figure 1.

The catenary action in the restrained beams starts as the axial force changes from negative to positive. This occurs at around 920 ℃ for austenitic beams, about 720 ℃ for the carbon steel beams, and around 690 ℃ for the duplex beams. These values correspond to temperature levels at which large deflection was observed in the beams as identified previously based on the V4 results plotted in Figure 23.

The displacement and axial force results suggest that the structural fire performance of the frames was dominated by the column behaviour. The catenary action in the frame beam occurred when the large deflection was induced because of thermal expansion against the restraints.

Figure 26 presents the midspan deflection (V4) of the beams under the L.R.=0.6 with varying degrees of external restraints. The corresponding vertical displacements of the columns under the L.R.=0.3 are plotted in the Figure 27. Similar results to the Figure 23 and Figure 24 were observed. As the L.R. increased from 0.15 to 0.3, the collapse temperature for the restrained columns reduced from 880 ℃ to around 650 ℃ for the austenitic, from 620 ℃ to 520℃ for the carbon steel, and from 560 ℃ to 200 ℃ for the duplex. The larger reduction in the collapse temperatures observed for the stainless columns are caused by the significant reduction in the tangent modulus at higher L.R.s.
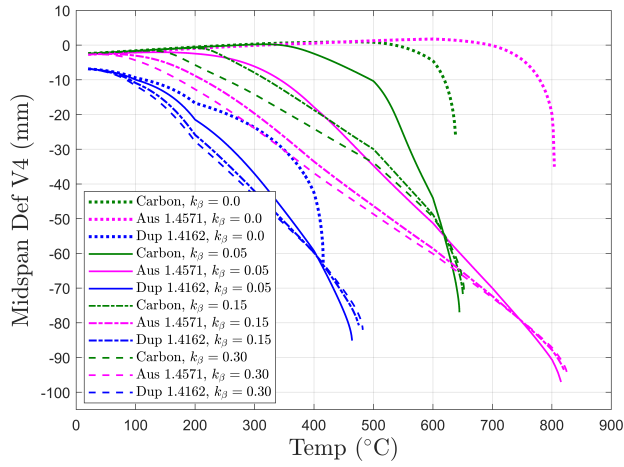
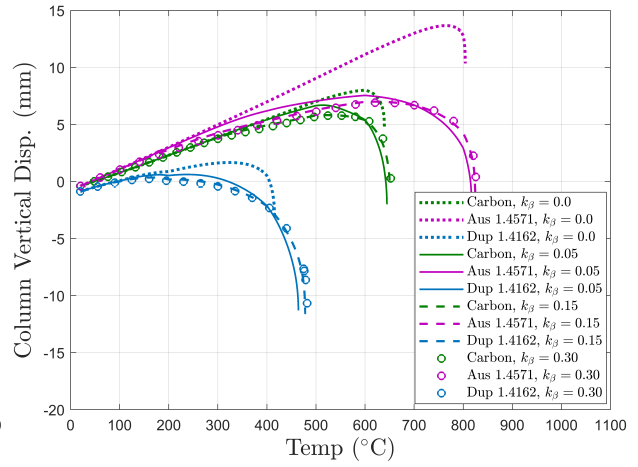**Figure 26:** Beam midspan def vs. temp, Beam L.R.=0.60

Figure 27: Column vertical disp vs. temp, Column L.R.=0.30

Figure 28 presents the stress-strain developments at the beam-column joint during the fire , in the cross-section of the beam and the column respectively. An initial negative bending moment —bottom flange in compression while top flange in tension is observed in the beginning of the fire due to the $P - \delta$ effect of the initial beam deflection. During heating, compressive stresses developed across the entire cross section, manifested as the tensile stress at the top shifted to the compressive side and the compressive stress at the bottom increased until the occurrence of the collapse. Higher peak stresses were observed for the case of $0.15K_\beta$ restraint when compared to the $0.05K_\beta$ restraint case.

Figure 28a and 28b show that the strain reversals were clearly experienced at the beam-column joint, in both beams and columns. This occurrence demonstrated that the strain reversals would occur with the presence of axial restraints within the structure.
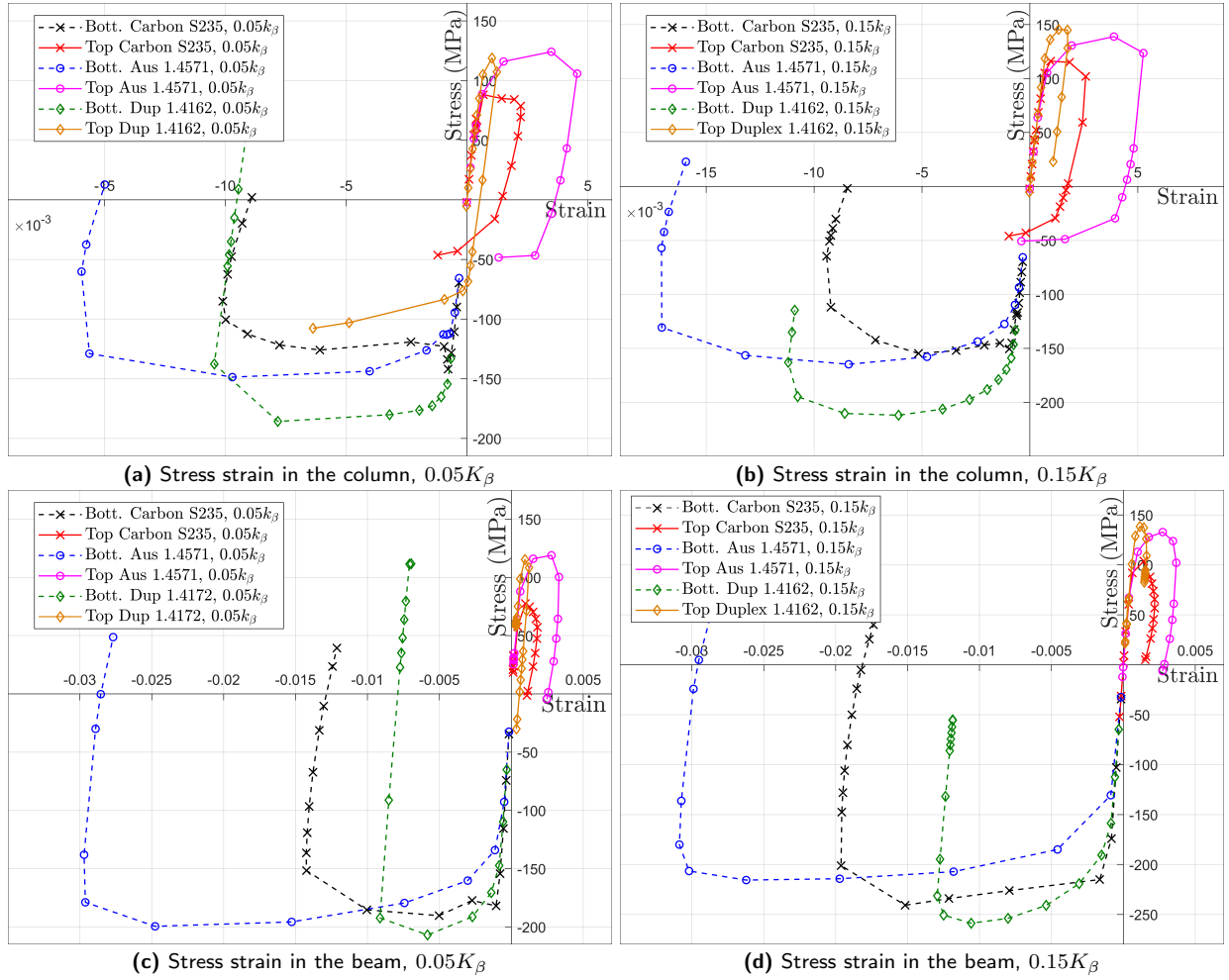
(a) Stress strain in the column, $0.05K_\beta$

(b) Stress strain in the column, $0.15K_\beta$

(c) Stress strain in the beam, $0.05K_\beta$

(d) Stress strain in the beam, $0.15K_\beta$

Figure 28: Stress strain developments at beam-column joint, Beam L.R.=0.30, Column L.R.=0.15

The comparison study showed that for structural fire performance, the inclusion of external restraints is detrimental to the columns because it accelerates the initiation of the column collapse; meanwhile beneficial to the beams since it enables the catenary action. The stress redistributions due to the catenary action subsequently result in strain reversals in the structure. Increasing the stiffness level of restraints showed little impact on the column collapse temperature, however it induced higher stresses in the frame.

7. Conclusions

The capability of the new material model of Zhou et al. [4] has been further validated for transient loading conditions during heating and cooling. The new material model's capability for post-fire structural assessment has been demonstrated. The material model has been specialised into a 1D J2 plasticity model and implemented in OpenSEES for studying the stainless steel structural behaviour in fire.

The comparison study of temperature development between carbon steel and stainless steel I-sections subjected to four sides heating of the Standard Fire Curve [35], demonstrated a slower temperature rise for the stainless steel sections. For thin-walled structures, lower emissivity is the main beneficial factor that stainless steel offers. The comparison study results have shown that sections with a smaller section factor (A/V) benefit more from using stainless steels in terms of achieving a slower temperature development.

The comparison study of simply supported beams suggest that the Austenitic 1.4571 stainless steel can generally postpone the onset of large deflection mechanism in the beam to a temperature of more than 200 °C higher than that of the carbon steel. At higher L.R.s (L.R.¿0.75), the deflection rate of austenitic beams are significantly faster than that of carbon steel beams due to the reduction in its tangent stiffness modulus, which can quickly reduce to about 50% of the material's initial value when stress approaches 50% of the strength capacity.

Similarly, the Duplex 1.4612 stainless steel showed the capability of delaying the large deflection mechanism of the simply supported beams during the heating when L.R. is low (< 0.36). The Duplex 1.4612 steel experiences substantial reduction in the tangent modulus when L.R. exceeds 0.50, which accelerates the onset of large deflection mechanism.

The comparison of EHR3 frames have shown that the Austenitic 1.4571 steel offers a clear advantage in delaying the occurrence of frame collapse, and the degree of advantage diminishes as the L.R. increases. The Duplex 1.4612 steel only showed benefits of postponing the collapse of EHR3 frame in the Series 1 study where the L.R. is 0.15 in the beam and 0.075 in the column. The advantage offered by the Duplex 1.4612 steel is believed probably uneconomic because of the low L.R.s that have to be maintained.

The comparison study results show that the introduction of axial restraints at the beam-column joint of the EHR3 frame cause earlier column collapse, where the stainless steels suffer greater decrease in the collapse temperature when compared to the carbon steel.

The catenary action is beneficial for structural fire performance of frames. However the strain reversals experienced during the catenary action can cause reduction in the material tensile strength due to the Bauschinger effect. Future investigation of the Bauschinger effect on the structural behaviour of steel structures in fire using the new material model is of great research interest.

The effect of substantial plastic hardening in stainless steel structures on the structural performance during the cooling stage of a fire should also be investigated in the future.

References

[1] Specification for the Design of Light Gauge Cold-Formed Stainless Steel Structural Members (1968).

[2] Design Manual for Structural Stainless Steel (2017).

[3] B. R. E. Ltd, Results and observations from full-scale fire test at BRE Cardington (Jan 2003).

[4] M. Zhou, R. Cardoso, H. Bahai, A new material model for thermo-mechanical analysis of steels in fire, International Journal of Mechanical Sciences 159 (2019) 467 – 486 (2019).

[5] N. Ohno, R. Yamamoto, D. Okumura, Thermo-mechanical cyclic hardening behavior of 304 stainless steel at large temperature ranges: Experiments and simulations, International Journal of Mechanical Sciences 146-147 (2018) 517 – 526 (2018).

[6] F. McKenna, Opensees: A framework for earthquake engineering simulation, Computing in Science Engineering 13 (4) (2011) 58–66 (July 2011).

[7] Kim J.R. Rasmussen, Full range stress-strain curves for stainless steel alloys, Journal of Constructional Steel Research 59 (1) (2003) 47 – 61 (2003).

[8] I. Arrayago, E. Real, L. Gardner, Description of stress-strain curves for stainless steel alloys, Materials and Design 87 (2015) 540–552 (2015).

[9] M. Dundu, Evolution of stress - strain models of stainless steel in structural engineering applications, Construction and Building Materials 165 (2018) 413 – 423 (2018).

[10] E. Silvestre, J. Mendiguren, L. Galdos, E. S. de Argandona, Comparison of the hardening behaviour of different steel families: From mild and stainless steel to advanced high strength steels, International Journal of Mechanical Sciences 101-102 (2015) 10 – 20 (2015).

[11] A. Olsson, Stainless steel plasticity - material modelling and structural applications, Ph.D. thesis, Lulea University of Technology (2001).

[12] J.Gozzi, Plastic behaviour of steel: Experimental invesitgation and modelling, Ph.D. thesis, Lulea University of Technology (2004).

[13] Eurocode 3 : Design of steel structures - Part 1-2: General rules -Structural fire design (2005).

[14] G. Gedge, Structural uses of stainless steel - buildings and civil engineering, Journal of Constructional Steel Research 64 (11) (2008) 1194–1198 (2008).

[15] P.Ludwik, Elemente der Technologischen Mechanik, Springer, Berlin, 1909 (1909).

[16] A. Phillips, C. S. Liu, J. W. Justusson, An experimental investigation of yield surfaces at elevated temperatures, Acta Mechanica 14 (2) (1972) 119–146 (Jun 1972).

[17] M. B. D. Harley, E.J; Miller, Experimental Study of Internal Variable Evolution in SS304L , at Multiple Rates and Temperatures, Journal of Engineering Materials and Technology 121 (2) (1999) 162–171 (1999).

[18] K. Maciejewski, Y. Sun, O. Gregory, H. Ghonem, Time-dependent deformation of low carbon steel at elevated temperatures, Materials Science and Engineering: A 534 (2012) 147 – 156 (2012).

[19] D. Drysdale, An Introduction to Fire Dynamics: Third Edition, Wiley Blackwell, 2011 (2011).

[20] S. Welch, A. Jowsey, S. Deeny, R. Morgan, J. Torero, Bre large compartment fire tests - characterising post-flashover fires for model validation, Fire Safety Journal 42 (8) (2007) 548 – 567 (2007).

[21] R. D. Krieg, A practical two surface plasticity theory, Journal of Applied Mechanics 42 (3) (1975) 641 (1975).

[22] Y. F. Dafalias, E. P. Popov, Plastic internal variables formalism of cyclic plasticity, Mechanics Research Communications 3 (1) (1976) 33–38 (1976).

[23] E. Voce, A practical strain hardening function, Metallurgia 51 (1955) 219–226 (1955).

[24] W.-W. Yu, R. A. LaBoube, Cold-formed steel design, John Wiley & Sons, Inc., 2010 (2010).

[25] X. Qiang, F. S. Bijlaard, H. Kolstein, Post-fire mechanical properties of high strength structural steels s460 and s690, Engineering Structures 35 (2012) 1 – 10 (2012).

[26] X. Qiang, F. S. Bijlaard, H. Kolstein, Post-fire performance of very high strength steel s960, Journal of Constructional Steel Research 80 (2013) 235 – 242 (2013).

[27] W. Wang, T. Liu, J. Liu, Experimental study on post-fire mechanical properties of high strength q460 steel, Journal of Constructional Steel Research 114 (2015) 100 – 109 (2015).

[28] F. Azhari, A. Heidarpour, X.-L. Zhao, C. R. Hutchinson, Mechanical properties of ultra-high strength (grade 1200) steel tubes under cooling phase of a fire: An experimental investigation, Construction and Building Materials 93 (2015) 841 – 850 (2015).

[29] X. Wang, Z. Tao, T. Song, L. Han, Stress strain model of austenitic stainless steel after exposure to elevated temperatures, Journal of Constructional Steel Research 99 (2014) 129 – 139 (2014).

[30] Z. Tao, X. Wang, M. K. Hassan, T. Song, L. Xie, Behaviour of three types of stainless steel after exposure to elevated temperatures, Journal of Constructional Steel Research 152 (2019) 296 – 311 (2019).

[31] Y. Huang, B. Young, Post-fire behaviour of ferritic stainless steel material, Construction and Building Materials 157 (2017) 654 – 667 (2017).

[32] Y. Huang, B. Young, Mechanical properties of lean duplex stainless steel at post-fire condition, Thin-Walled Structures 130 (2018) 564 – 576 (2018).

[33] F. Azhari, A. H., X. Zhao, C. Hutchinson, Post-fire mechanical response of ultra-high strength (grade 1200) steel under high temperatures: Linking thermal stability and microstructure, Thin-Walled Structures 119 (2017) 114 – 125 (2017).

[34] L. Gardner, K. Ng, Temperature development in structural stainless steel sections exposed to fire, Fire Safety Journal 41 (3) (2006) 185–203 (2006).

[35] Iso 834, fire-resistance tests.

[36] A. Rubert, P. Schaumann, Structural steel and plane frame assemblies under fire action, Fire Safety Journal 10 (3) (1986) 173–184 (may 1986).

[37] Compendium of UK Standard Fire Test Data - Unprotected Structural Steel -1, Tech. rep., UK Department of the Environment Fire Research Station; British Steel Corporation (1988).

[38] N. Baddoo, Stainless steel in construction: A review of research, applications, challenges and opportunities, Journal of Constructional Steel Research 64 (11) (2008) 1199–1206 (2008).

Appendix A. Numerical Algorithm for One-dimensional Combined Isotropic and Kinematic Hardening Model

<hr>

Last Converged Step n

If Temperature change $\Delta T \neq 0$, Go to Thermal Step, Else Go to Mechanical Step

<hr>

Thermal Step, Current Temperature T_{n+1}

<hr>

1. Update Temperature dependent Parameters

Young's modulus E_{Tn+1}, Initial yield stress $\sigma_{p,Tn+1}$

Hardening function parameters v_{Tn+1} and δ_{Tn+1}

Bauschinger ratio evolution equation parameters a_{Tn+1}, b_{Tn+1} and c_{Tn+1}

2. Update Bauschinger ratio: $\vartheta_{Tn+1} = a_{Tn+1} * exp(-b_{Tn+1} * \overline{\varepsilon^p}_n) + c_{Tn+1}$

3. Update the size of bounding surface

$$Y = Y_{1D,Tn+1}(\overline{\varepsilon^p_n})$$

4. Update the position of the yield surface centre, β_1 term

$$\beta_{1n} = (1.0 - \vartheta_{Tn+1})Y sign(\varepsilon^p_n)$$

<hr>

Mechanical Step, Strain Increment $\Delta\varepsilon$

<hr>

1. Elastic predictor

$\sigma_{n+1}{}^{trial} = E_{n+1} \cdot (\varepsilon_n + \Delta\varepsilon - \varepsilon^p_n)$, $\quad \beta_{1}{}^{trial}_{n+1} = \beta_{1n}$, $\quad \beta_{2}{}^{trial}_{n+1} = \beta_{2n}$

$\eta^{trial}_{n+1} = \sigma^{trial}_{n+1} - \beta_{1}{}^{trial}_{n+1} - \beta_{2}{}^{trial}_{n+1}$,

$\vartheta_{n+1} = a_{n+1} * exp(-b_{n+1} * \overline{\varepsilon^p}_n) + c_{n+1}; \qquad \nu_{n+1} = 1.0 - exp(-b_{n+1} * \overline{\varepsilon^p_l}_n)$

Reverse loading index : $l^{trial}_{n+1} = l_n; \qquad \overline{\beta_l}{}^{trial}_{n+1} = \overline{\beta_l}_n$

- Check the reverse loading criterion

If $cos(\theta) < 0.0$ then

$l^{trial}_{n+1} = l_n + 1; \qquad \overline{\varepsilon^p}{}^{trial}_{l\,n+1} = 0.0; \qquad \overline{\beta_l}{}^{trial}_{n+1} = Vr_{Tn+1}|\beta_{1n} + \beta_{2n}|; \qquad \beta_{2}{}^{trial}_{n+1} = 0.0$

Else, Do nothing

- Check the yield condition

If $f(\eta^{trial}_{n+1}) - \vartheta_{n+1}Y_{1D,n+1}(\overline{\varepsilon^p}) < Tolerance$, then Set $(\bullet)_{n+1} = (\bullet)^{Trial}$ Exit

Else Go to Plastic corrector

2. Plastic corrector

- Newton-Raphson iteration is employed to determine plastic multiplier $\Delta\gamma$. Initialise $\Delta\gamma = 0.0$

Iterate until $|g(\Delta\gamma)| < Tolerance$

$g(\Delta\gamma) = |\eta_{n+1}^{trial}| - 2 * \mu_{n+1} * \Delta\gamma - \vartheta_{n+1} * Y_{1D,n+1}(\overline{\varepsilon_n^p} + \Delta\gamma)$

$dg(\Delta\gamma) = -2 * \mu_{n+1} - [Y'_{1D,(n+1)}(\overline{\varepsilon_n^p} + \Delta\gamma)] * \vartheta_{n+1}$

Y' is the first derivative of Y with regard to $\Delta\gamma$

$\Delta\gamma = \Delta\gamma - g/dg$

○ ϑ_{n+1} is considered a constant during the Newton-Raphson iteration for small step of $\Delta\gamma$.

The consequent 'residual stress' of this simplification will be solved in the next iteration.

3. Update stress state

$\varepsilon^p{}_{n+1} = \varepsilon^p{}_n + \Delta\gamma sign(\eta_{n+1}^{trial}); \qquad \overline{\varepsilon_{n+1}^p} = \overline{\varepsilon_n^p} + \Delta\gamma; \qquad \overline{\varepsilon_{l(n+1)}^p} = \overline{\varepsilon_{l\,n+1}^{p\,trial}} + \Delta\gamma$

$l_{n+1} = l_{n+1}^{trial}; \qquad \vartheta_n = c + a * exp(-b * \overline{\varepsilon_n^p}); \qquad \vartheta_{n+1} = c + a * exp(-b * \overline{\varepsilon_{n+1}^p})$

If $l_{n+1} \neq 0$ then

$\nu_n = 1 - exp(-b * \overline{\varepsilon_{l\,n}^p}); \qquad \nu_{n+1} = 1 - exp(-b * \overline{\varepsilon_{l\,(n+1)}^p})$

$\overline{\beta_2} = (\nu_{n+1} - \nu_n) * \overline{\beta_{l\,n+1}^{trial}}; \qquad \beta_{2\,n+1} = \beta_{2\,n+1}^{trial} + \overline{\beta_2} sign(\eta_{n+1}^{trial})$

Endif

$\beta_{1\,n+1} = \beta_{1\,n+1}^{trial} + [(1 - \vartheta_{n+1})Y_{n+1}(\overline{\varepsilon_{n+1}^p}) - (1 - \vartheta_n)Y_{n+1}(\overline{\varepsilon_n^p})]sign(\eta_{n+1}^{trial})$

$\sigma_{n+1} = \sigma_{n+1}^{trial} - 2 * \mu_{n+1} * \Delta\gamma sign(\eta_{n+1}^{trial})$

Appendix B. Tables of Parameters

Table B.13: Least Square Fitting Results for Hardening Law - St 37.2 Carbon Steel in [36]

Temperature (℃)	σ_{0_T}	v_T	δ_T	Adj-R-sq
100	250.0	0.0	-	-
200	226.4	23.61	22.84	0.980
300	158.5	90.58	23.62	0.988
400	143.6	105.5	24.42	0.982
500	129.5	56.57	25.03	0.991
600	56.58	67.48	24.27	0.990
700	22.1	39.67	23.97	0.991

Table B.14 presents the curve fitting results of v_T and δ_T for every 100 ℃. Linear interpolation will be used to obtain the intermediate values.

Table B.14: Least Square Fitting Results for Hardening Law - EC3 carbon steel

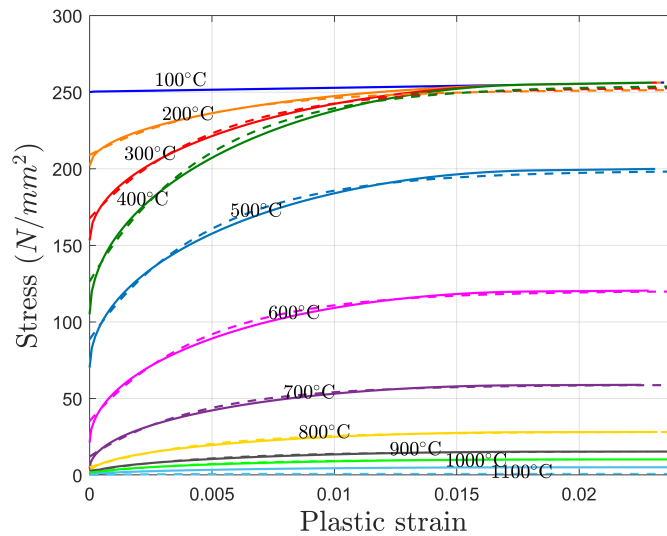| Temperature (℃)	v_T	δ_T	Adj-R-sq
100	0.0	-	-
200	48.1	168.5	0.996
300	90.9	187.8	0.996
400	133.6	198.5	0.996
500	114.6	197.8	0.996
600	87.8	206.2	0.995
700	48.3	213.9	0.995
800	23.7	202.5	0.995
900	13.1	195.9	0.995
1000	8.9	196.1	0.995
1100	0.9	196.3	0.995

Figure B.29: EC3 stress-strain curves v.s. Least square fitting

For the paper with title: "**A thermo-mechanical analysis of stainless steel structures in fire**", the authors declare no conflicts of interests.
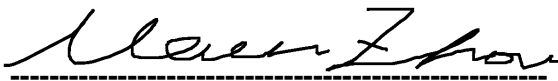
Author Statement

The work submitted in the manuscript entitled "A thermo-mechanical analysis of stainless steel structures in fire" was carried out Mian Zhou, under the supervision of the co-authors. This work is not funded.

Sincerely,

Mian Zhou

London, 2rd of December of 2019

Department of Mechanical and Aerospace Engineering
Brunel University London
Kingston Lane, Uxbridge, UB8 3PH
Unite Kingdom
E-mail: mian.zhou@yahoo.com